UNIVERSITY OF OSLO

Department of Physics

Oxygen Dimers in Solar Cell Silicon studied by Fourier Transform Infrared Spectroscopy

Master thesis

Anne Skogstad

1st June 2011

"Believe you can and you're halfway there."

-Theodore Roosevelt

Acknowledgments

First of all, I would like to thank my supervisor Professor Bengt Svensson for giving me the opportunity to work in the exiting and interesting field of semiconductor physics, and for all help and interesting discussions.

Special thanks goes to Leonid Murin for all help and support, Eduard Monakhov for letting me go to the Nordic workshop on defect engineering of silicon, and Bahman Raeissi for all help with my thesis.

A big thanks goes to Viktor Bobal for all the helpful repair of the FTIR and for the help in the clean room, Halvard Haug for introducing me to the FTIR and Hans Bjørge Normann for all help and support when I was at my most frustrating moments.

I also want to thank all the people at MiNaLab for all the support and for making this a very nice experience in a great environment. Thanks to Frode Kløw, Per Lindberg and Matthew Schofield for making every day interesting at the "kinder garden" and for very appreciated friendships.

My family deserves a big thanks, specially Marie, who pushed me in the right direction and always believed in me. A very special thanks to Frode for all the support and help throughout these years, and for being the most incredible person in my life. I could not have done this without you.

Anne Skogstad, Oslo, May 2011

Abstract

Oxygen defects in Czochralski grown n-type silicon solar cell material were investigated with Fourier transform infrared spectroscopy (FTIR). Samples were annealed at fixed temperatures ranging from 300-470°C.

Different vibrational and electronic transition bands could be seen, like the VO_2, VO_3 and VO_4 vibrational bands at room temperature measurements. The increase in VO_3 band had a linear dependence with decreasing VO_2 band throughout the annealing.

When oxygen rich silicon is annealed, thermal double donors (TDDs) appear in the material, which degrade the solar cell performance. Oxygen dimers are believed to be a precursor for TDDs and their vibrational bands at 556, 1012 and 1060 cm^{-1} were monitored by FTIR. The dimer concentration were found and showed an exponential dependency with annealing time. The activation energy was extracted by first order kinetics to be around 1.4-1.6 eV and assigned to the dimer diffusion with a diffusion pre-factor, D_0, of 5.5×10^{-3}-5.0×10^{-2} cm^2/s.

After annealing, four point probe measurements were done and showed a decrease in resistivity, which means that the annealed samples had become more n-type, due to increase of TDD complexes.

Contents

Chapter 1

Introduction

The main energy sources today are oil, coal and gas. These sources are not renewable and they will come to an end some time in the future. The demand for energy keeps growing and it is therefore necessary to find new energy sources that can fill our need for energy. Solar energy has become an interesting alternative as an energy source in today's society. When oil, gas and coal are limited resources, solar energy is a renewable resource that does not pollute the environment. Solar cells have emerged as a good alternative to produce electricity in an environmentally friendly way.

The most used material for making solar cells is silicon that is the most important and widely used semiconductor material today. It can be found in large amounts on earth and is also cheap to extract. Still there are other limitations for silicon as a solar cell. A perfectly made single-crystal Si solar cell can have about 30% efficiency for solar energy conversion. This gives approximately 250 W/m^2 electrical power under full illumination [1]. Since most solar cells are not perfectly made, there is ongoing research on improving the silicon solar cell, as well as finding new and better materials to use as solar cell material.

This thesis is going to look at one of the problems that degrades silicon solar cells. When the silicon solar cell material has been annealed, electrical

active centers appear, that have a detrimental influence on the performance of the solar cell. These defects come from oxygen incorporated in the silicon crystal. Oxygen has an influence on the electrical and mechanical properties of the silicon material, and some of these effects are not desired in a solar cell. This thesis will study oxygen dimer defects in silicon material grown by the Czochralski (Cz) pulling method. Dimers come from the high concentration of oxygen in the silicon crystal, that originates from the quartz crucible that is used in the Cz pulling method to contain the melted silicon [2]. It is believed that oxygen dimers are the precursors for some of the detrimental defects that are found in Cz silicon.

When infrared (IR) spectroscopy techniques were taken in use for silicon measurements, the research on oxygen defects escalated. It began in 1950s [3, 4] and is still an important research subject. There are a lot of questions about oxygen defects in silicon that are still not answered. This thesis will look at oxygen dimers in electron irradiated and annealed samples with Fourier transform infrared spectroscopy (FTIR). The focus will be on dimer absorption bands, how they change with annealing time and how the dimer concentration changes with temperature. A preliminary value of the activation energy for the diffusion of dimers will be deduced.

Chapter 2

Background

2.1 Basic Theory

In this chapter a short introduction to crystal and semiconductor theory, with the main focus on silicon materials, will be given. The sections on crystal and defect theory are based on the textbooks of solid state physics by Kittel [5] and material science by Tilley [6]. The sections on semiconductor theory are based on the textbooks of Streetman [1] and Kittel [5]. For further theory the reader is referred to these books or other text books on the subject.

2.1.1 Crystal theory

When atoms in a material have a long range order, the material is called a crystal. A crystal lattice consists of infinite positions that have the same surroundings in the same orientation. These points can be described by some simple vectors. If any lattice point is chosen to be origin, then the point is defined by P(u v w) = u$\mathbf{a}$ + v$\mathbf{b}$ + w$\mathbf{c}$, where $\mathbf{a}$, $\mathbf{b}$ and $\mathbf{c}$ are the basis vectors and u, v and w are positive or negative integers. The cell formed by the basis vectors is called the unit cell, which is the most basic structural element, and it describes the smallest repeating unit in the crystal.

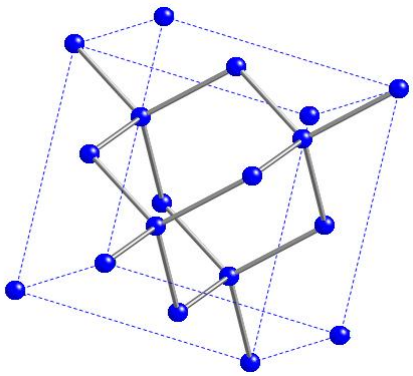

Figure 2.1: The silicon crystal structure.

There are 14 possible three-dimensional lattices, called Bravai lattices. All types of crystal structures can be built up from these, by placing atoms or groups of atoms in the lattice points, which are called the basis of the crystal structure.

Silicon has a face-centered cubic structure also called diamond structure, see figure 2.1. The bravai lattice is face-centered cubic and there are two silicon atoms in the basis and each silicon atom is bonded to four others with bond length of $a_0 = 0.542$ nm.

2.1.2 Defect theory

There is no such thing as a perfect crystal. All types of crystals have some sort of defects due to entropy. According to thermodynamic laws entropy can only increase, which happens in the presence of disorder in the crystal, like impurity atoms or lattice defects.

Defects are often divided into point-, line- and bulk defects. Point defects are one-dimensional defects and the most simple one is the lattice vacancy (V), as shown in figure 2.2a, which is an empty site in the lattice. There are two types of V defects, Schottky and Frenkel defects. The former is created by taking an atom out of its position in the lattice to the surface. In the latter an atom is taken out of its place in the lattice and pushed into

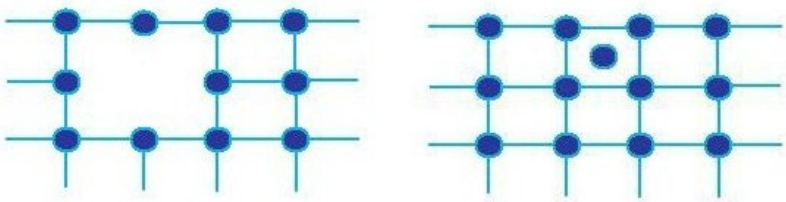

(a) Vacancy (b) Interstitial

Figure 2.2: Two important point defects when studying defects in silicon crystals.

an interstitial position. An interstitial position is a site in the lattice that normally is not occupied by an atom. The atom in this site is called an interstitial atom (I) which is also a point defect, see figure 2.2b. When the atom is of the same type as the one in the crystal lattice, the defect is called a self interstitial. Another type of point defect is a substitutional atom, which is an impurity atom incorporated in the lattice. Impurity atoms can also occupy interstitial sites in the lattice.

Line- and bulk defects are two- and three-dimensional defects, respectively. These defects are more complex and extended than point defects. An example of a line defect is edge dislocation which is an extra plane inserted between to crystal plains in the crystal. There can also be clusters of defects in a crystal, like precipitates that are impurity or host atoms coming together to form three dimensional clusters.

2.1.3 Semiconductor theory

Solids can be divided into metal, insulator and semiconductor depending on their electrical properties. The main difference is that a metal is electrically conducting, while an insulator is not. The semiconductor, however, experiences both metal- and insulator properties under different conditions. These properties come from the quantized bond structure of electrons in the

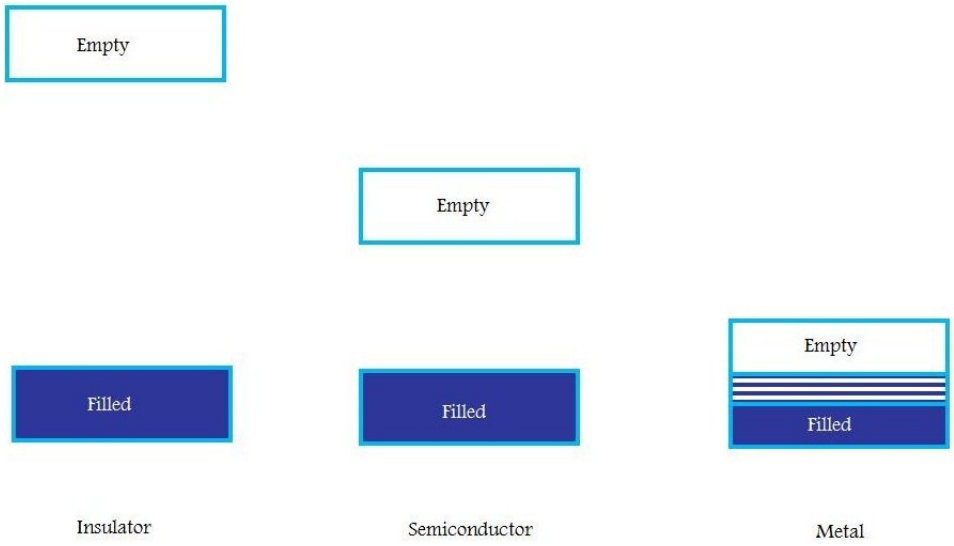

Figure 2.3: A schematic overview over the band gaps of insulator, semiconductor and metal.

compound.

When atoms come together, the electrons make bonds between the atoms to make a compound. These electrons can only occupy allowed bond states and between these states forbidden gaps occur called band gaps, E_g. In a metal, the upper most filled band is not completely filled, giving room for electrons to move when an electric potential difference is applied across the material, making the material conducting. In the case of an insulator the upper most filled band is nearly filled, and the electrons are tightly bonded to their atoms. The next band lies so high in energy that the electrons can not be excited up. However, if the band gap is small and the electrons are given enough energy corresponding to the band gap, they can be excited to the next band and the material can now conduct. In this case the material is a semiconductor. The upper band over the band gap is called the conduction band, E_c, and the lower band is called the valence band, E_v. In figure 2.3 a schematical view over the band gaps of metal, insulator and semiconductor are shown.

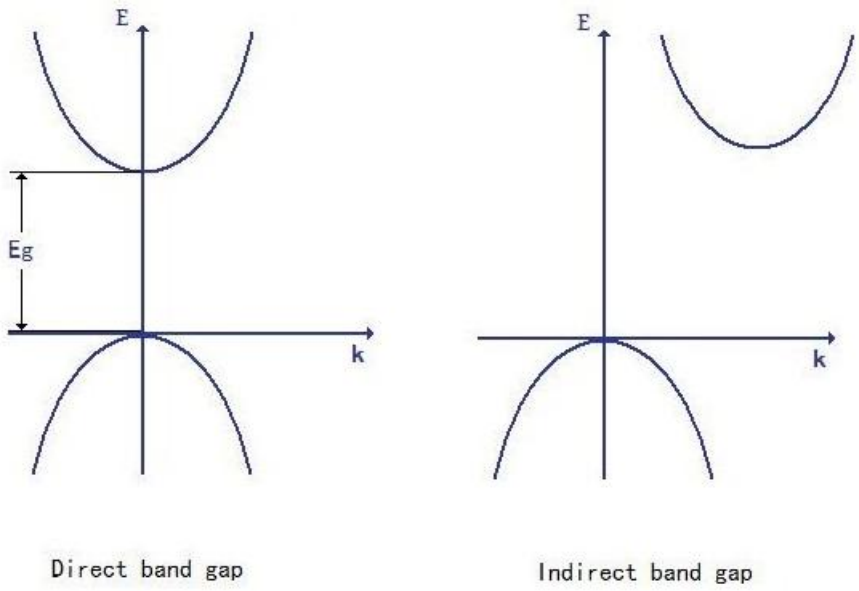

Figure 2.4: A schematic view over direct and indirect band gaps. Indirect band gaps need heat in addition to, for example, light to excite electrons to the conduction band.

An electron is excited to the conduction band, directly from the valence band, by absorbing a photon with energy

$$E_{\mathrm{g}} = hv, \tag{2.1}$$

where h is Planck constant and v is frequency. This type of band is called a direct band gap. In some cases the electron also needs a change in wave vector to be excited. These band gaps are called indirect band gaps and heat in addition to photon energy can be used to excite electrons. Figure 2.4 shows schematically the difference between an indirect and a direct band gap. For example, silicon has an indirect band gap of 1.11 eV and GaAs has a direct band gap of 1,43 eV, at room temperature.

When an electron is excited to the conduction band a hole is left in the valence band. These electron-hole pairs are called excitons and are held to-

gether by their attractive coulomb interactions. The electrons can recombine with the holes either in direct- or indirect ways. In direct recombination, the electron goes directly back to the valence band to annihilate the hole and the energy is commonly released as a photon. In the indirect way the electron needs to go trough recombination centers that appear in the band gap, before it can recombine with the hole in the valence band. The energy is commonly lost by heat to the crystal lattice. Recombination centers can often come from impurities or lattice defects in the material and are usually not desired. The average time that an electron and a hole uses to recombine is called the carrier lifetime.

2.1.4 Doping

Impurities and imperfections can affect the electrical properties of a semiconductor. Impurity atoms that are intentionally introduced into a material for changing the conductivity are called dopants.

A semiconductor is p-type when doped with elements from the III-group of the periodic table. Boron, aluminum, gallium and indium are often used and are called acceptors. They generate states in the band gap as drawn in figure 2.5a, that lie near the valence band. Electrons can be excited into these states and leave holes in the valence band.

When a semiconductor is doped with elements from the V-group of the periodic table, it is called n-type. These dopants are called donors, and phosphorus, arsenic and antimony are commonly used. Their states are found near the conduction band in the band gap, see figure 2.5b, and have extra electrons that can be donated to the conduction band by thermal excitation.

In a n-type material, the density of electrons in the conduction band is larger than that of holes in the valence band. Therefore electrons dominate and are the majority carriers. In p-type material, holes are the majority

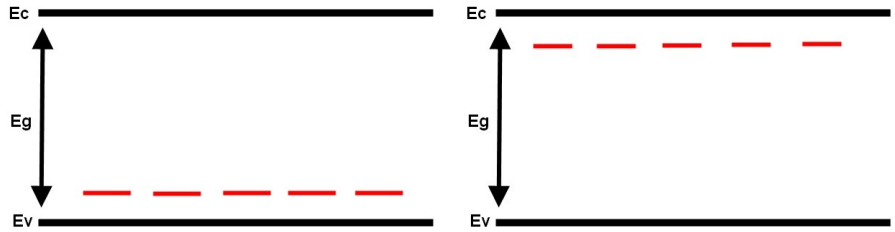

(a) Acceptor (b) Donor

Figure 2.5: The red lines in the figures represent the acceptor and donor levels in the band gap.

carriers.

Normally in a semiconductor crystal, both donors and acceptors are present, and the one with the larger concentration makes the semiconductor p- or n-type. The two different doping types can compensate each other. This means that the majority doping can be reduced by the minority doping.

2.1.5 Solar cell

A solar cell is a photovoltaic cell with the ability to convert solar radiation into electricity. A photovoltaic cell is made by connecting a p-type and a n-type semiconductor together to form a p-n-junction, as shown in figure 2.6. When the two doped materials join together, majority carriers start to diffuse to the other side, because of the difference in electron and hole concentration. By diffusing to the other side, holes and electrons leave uncompensated acceptors and donors at the edge where the two materials come together, called the depletion region, in which an electric field arises. This electric field creates a drift of carriers in the opposite direction of the diffusion until equilibrium is reached.

When the p-n junction is illuminated near and in the depletion region, more electrons and holes are generated. By the electric potential difference, they will be separated and swept over the junction to be collected as electric

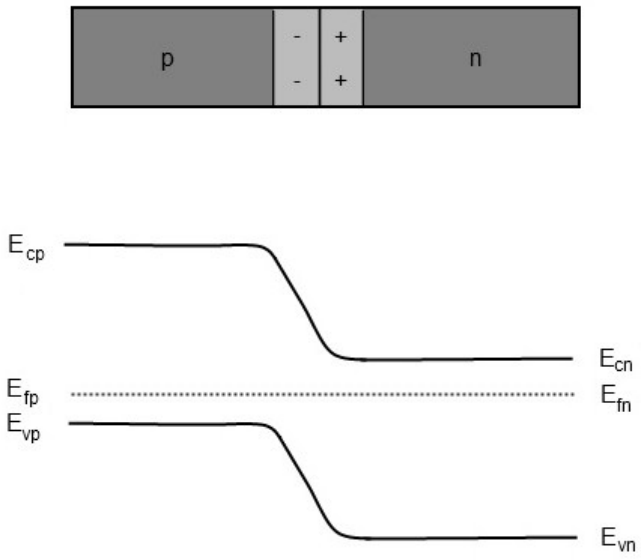

Figure 2.6: P-n-junction.

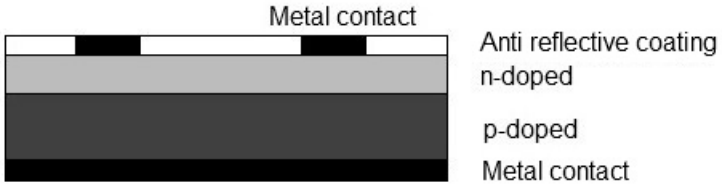

Figure 2.7: A basic solar cell structure.

current. Figure 2.7 shows a scematic solar cell with a p-n junction, metal contacts to collect the current, and an anti-reflective coating to prevent reflection of the incoming light and surface recombination.

2.2 Silicon theory

This chapter will go through basic silicon theory, how silicon is extracted and the most popular method for growing crystalline silicon. It is based on the book "Oxygen in Silicon" edited by Shimura [2].

2.2.1 Basic theory of silicon

Silicon is a group IV element in the periodic table and is widely used in semiconductor industry. There are several types of natural compounds that contain silicon. The most abundant is SiO_2, also known as quartz, and pure silicon can be extracted in the following way. SiO_2 is reacteded with carbon in the form of coke at high temperatures,

$$SiO_2 + 2C \rightarrow Si + 2CO \tag{2.2}$$

which forms metallurgical grade Si (MGS) with a purity of about 97%. MGS contains impurities like iron and aluminum in the amount of several hundred to several thousand parts per million. For solar cell application, MGS must be purified, therefore the next step in the process is to make it react with dry HCL,

$$Si + 3HCl \rightarrow SiHCl_3 + H_2. \tag{2.3}$$

Then, the $SiHCl_3$ is distilled by a technique called fractional distillation to remove impurities by a reaction with H_2, electronic grade silicon (EGS) is made,

$$2SiHCl_3 + 2H_2 \rightarrow 2Si + 6HCl, \tag{2.4}$$

which has a purity of about >99.9999%. EGS is mainly used for semiconductor technology and today most solar cell applications come from solar grade silicon which has a purity of about 99.99-99.999%. The resulting material from this fare in the process is polycrystalline and to make it monocrystalline, two methods called Czochralski pulling method and float-zone growth are used.

2.2.2 Czochralski pulling method

Cz pulling method is the most popular method to grow single crystal silicon. It is named after Jan Czochralski in 1918, but the method as it is today was invented in 1950 by Teal and Little [2]. Figure 2.8 shows a schematic overview over the Cz pulling process. Pure polycrystalline silicon and doping elements are melted in a silica crucible. A crystal seed of about 12 mm in diameter, is dipped into the melt. The seed is rotated and lifted up slowly from the melt and a necking process starts, which is a process where the crystal diameter is reduced to about 3 mm and the pulling speed is increased. This combination makes the silicon dislocation free after a few centimeters of growth. Then, the diameter is increased by "shoulder" growth until the desired diameter is reached and a large silicon rod can be made and cut into wafers.

From the Cz pulling method several impurities are incorporated into the crystal. Carbon and oxygen are the major impurities and come from the crucible and the vapor above the melt. The crucible that holds the melted silicon is made of SiO_2. Molten silicon will start to dissolve the crucible and silicon oxide is formed,

$$SiO_2 + Si = 2SiO. \tag{2.5}$$

Oxygen is in this way transferred to the melt. Most of the oxygen atoms evaporate from the surface, and some of them are incorporated into the silicon crystal through the crystal-melt interface. Oxygen defects influence

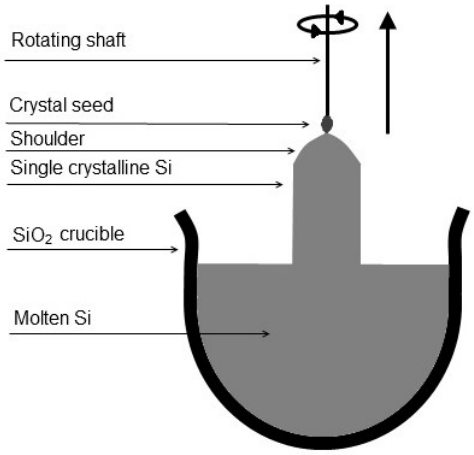

Figure 2.8: The Czochralski pulling method.

both the electrical and mechanical properties of silicon and mainly occupy interstitial sites in the silicon lattice. The oxygen concentration in silicon is about 10^{18} atm/cm^3.

Other impurities coming from the growing process are carbon impurities that come from the hot zone of the Cz grower, which contains graphite elements that are used to heat the crucible making the silicon melt. At the interface, between the hot zone and silicon, SiO reacts with the graphite and carbon impurities are transferred into the melt. The substitutional carbon concentration is about 10^{16} atm/cm^3 in the silicon crystal.

2.2.3 Float zone silicon growth

Another popular method for silicon crystal growing is the float zone (FZ) technique invented by Theuer in 1962 [2]. A polycrystalline silicon rod is held vertically in a growing camber and a coil provides radio frequency to the rod in order to make a molten zone. This zone is moved along the rod and at the same time the molten silicon starts to crystallize into a single crystal. The oxygen concentration is about 10^{16} atm/cm^3.

It is not possible to make large diameter crystals whit the FZ method, and the technique is more expensive than the Cz technique. This makes Cz the most popular technique even though it has a higher oxygen concentration.

2.2.4 Oxygen in silicon

Oxygen clusters can be beneficial to have in silicon. They act as traps for metal impurities, to prevent them from entering active device areas in the material. This process is called gettering and is used in microelectronic devices.

Oxygen incorporated in silicon crystals is not in general electrical active. They occupy interstitial sites (O_i) in the crystal at room temperature and form two strong bonds with two silicon atoms. When studying the material with IR spectroscopy the most important vibrational band is the on located at 1107 cm^{-1}, which is used for calculating the interstitial oxygen concentration.

When Cz-Si is annealed, oxygen starts to diffuse and make clusters that influence the electrical properties of the material. Oxygen atoms get thermal energy to form small electrical centers called thermal donors (TDs) which give rise to shallow donor states bellow the conduction band. Impurity donor states are not desirable due to change in the electrical properties of the material. They have extra electrons that are not bounded in the material and can be excited to the conduction band to change the conductivity. These states also act as traps for the recombination of electrons and holes, by making the electron go through several states before recombination. Unintentional doping can also compensate the intentional doping in the material. To overcome this issue, the material needs to be more heavily doped, which is not always desirable.

2.3 Crystal vibrations and electronic transitions

In IR spectroscopy, the light is transmitted through a sample and different wavelengths are absorbed. By plotting the absorption versus wavenumber, an absorption spectrum is made, which can be used to study defects in the material. In silicon there are three mechanisms for absorption of radiation in the intermediate region of the IR spectrum (between 400-4000 cm^{-1}). The first type is called lattice absorption, even though pure silicon is transparent in this region, there are lattice absorption bands that arise from phonon transitions. The second type is impurity absorption in the Si crystal mainly from oxygen, nitrogen and carbon impurities. The third type of absorption is from free-carriers [2].

Silicon has a high refraction index and the reflectivity is 0.300 [2] in the mid IR region. This means that about 70% of the incident light enters the silicon material and considering the internal reflections due to surfaces, about 50% is transmitted through the sample.

2.3.1 Vibrational modes in crystals

Atoms in a crystal are bonded together in a periodic fashion and vibrate in certain quantized vibrational modes. When IR radiation is absorbed in the crystal, transitions between quantized vibrational energies, occurs. These energies are called phonons. The vibrations that occur can range from a simple coupled motion to complex motions of larger molecules.

One atom has three *degrees of freedom*; it can vibrate in the three spatial dimensions. This gives the atom three vibrational modes. The degrees of freedom of a molecule are composed of vibration, translation and rotation. The vibrational modes of a molecule are therefore more complex than those of an atom. A diatomic linear molecule has six degrees of freedom where three are translation, one is vibration and two are rotation. For a non linear

molecule with N atoms the degree of freedom is given by [7]

$$3 + 3 + (3N - 6) = 3N \tag{2.6}$$

where there are three translation, three rotation and 3N-6 vibrational degrees of freedom.

For each mode the atoms will have their own characteristic frequency. For most vibrational modes, the energy difference between ground state and first excited state corresponds to the energy of radiation in the mid-infrared region. The energy of a mode with an angular frequency of ω is

$$E = (n + 1/2)\omega\hbar \tag{2.7}$$

where n is the quantum number of the excited states and $\hbar$ is the Planck constant divided by 2π [5].

When impurities are introduced into the crystal, both symmetry and vibration modes will be influenced. The modified modes can lie either within the perfect lattice frequency or new modes, that are higher, can appear. These modes are localized around the defect, and can absorb IR light at different frequencies compared to normal modes and are called localized vibrational modes (LVM).

2.3.2 Electronic transitions

When a semiconductor is doped or has energy states in the band gap due to defects, IR radiation can be absorbed under certain conditions. Donor and acceptor states in silicon that come from intentional doping are located around 0.03-0.06 eV from the band edges [1]. At low temperatures (LT), around 0 K, donor states in the band gap are filled with electrons and acceptor states are empty. The material needs only a small amount of energy to excite electrons from the donor states to the conduction band and from the valence band to the acceptor states. At room temperature (RT) the

thermal energy is kT = 0.0259 eV. TDs do not absorb IR radiation at RT and can only be seen in an IR spectrum measured at LT.

Chapter 3

Previous work

In this chapter a short overview of the research on oxygen defects in silicon will be presented with some theory of dimers and thermal donors. Also, there will be a section on hydrogen, carbon and boron related defects.

3.1 Thermal donors and dimers

3.1.1 Thermal donors

TDs that appear in silicon when annealed at temperatures around 300-600°C have been widely studied but the chemical nature and microscopic structure are still not fully understood. In this and the next sections some of the research on TDs and a model of TD formation will be presented that includes oxygen dimers.

Some of the first studies on oxygen in silicon and formation of TDs were done by Kaiser et al. [3, 4]. They did several investigations on silicon crystals with high oxygen concentration and found formation of electrical active TDs that appeared when the silicon crystal was annealed at 450°C. As the TD formation increased they found that the oxygen concentration decreased in the silicon crystal. They suggested that the oxygen atoms become mobile due to annealing and form complexes with the silicon atoms, which creates

energy states in the upper half of the band gap [4]. These complexes act as donors and are therefore called thermal donors. They can donate electrons to the conduction band and also act as recombination centers, changing the electrical properties of the material.

There are three different types of TDs based on the temperature range where they are formed, and where in the band gap they are. Bean and Newman [8] suggested that some of the TDs where thermal double donors (TDDs). These type of donors form in the temperature range 300-550°C and exist as several different TDD species. So far 17 different types of TDD ranging from TDD0 to TDD16 have been found [9, 10, 11]. For an extended view over TDDs and their peaks in the IR-spectrum, see Pajot "Optical absorption of impurities and defects in semiconducting crystals" [12].

At temperatures above 550°C the TDDs get annihilated with an activation energy of about 2.5 eV [13]. This is most likely due to the joining of more oxygen atoms on the pre-existing TD making it electrically inactive. These inactive TDs will break up, at higher temperatures between 650-850°C, and new donors (NDs) are formed [14, 15]. This is also recently confirmed by Singh et al. [16] where they conclude that oxygen-carbon complexes play an important role in ND formation.

The third type of TDs is called shallow thermal donors (STDs). Which give rise to IR bands at 150-300 cm^{-1} in an absorption spectrum. STDs appear after annealing at 450°C [17].

3.1.2 Thermal donor formation and dimers

There are several different models on the diffusion and formation kinetics of TDs, and it is not yet clear how the formation occurs. One of the biggest challenges related to TD formation was to link it directly to oxygen. Gösele and Tan [18] studied different models for oxygen diffusion in silicon and the formation of TDs. They suggested that TD formation comes from fast

diffusing oxygen-related species (FDS) in the material. One of their suggestions; the oxygen dimer (O_{2i}), that is a dioxygen complex, has been studied as a FDS [19].

The dimer structure and its mechanisms have been widely investigated [19, 20, 21, 22, 23], but not completely understood. The dimer structure is believed to exist in a *staggered* and a *square* (also known as *ring* or *skewed*) configuration. In the staggered configuration two O atoms have a common Si atom located in the same (110) plane [24]. In the square configuration two O atoms are separated by two Si atoms located in different (110) planes [21]. Changing from one configuration to another will lead to dimer diffusion in the silicon crystal [25] and can happen when the material is radiated with light. This could result in trapping of impurity atoms like boron to make complexes [26]. Recently Murin et al. [27] investigated p- and n-doped silicon with FTIR to find evidence of a square configuration, which they cold not. Therefore the model of dimer diffusion must be further investigated.

Dimers give rise to some vibrational bands in an IR spectrum located at 556, 690, 1012 and 1060 cm^{-1} [19]. They can be formed in different ways, and the most common one is when to interstitial oxygen atoms come together in the silicon material,

$$O_i + O_i \rightarrow O_{2i}. \tag{3.1}$$

At temperatures above 400°C, dimers are no longer stable and dissociate into TDs [3]. It is well accepted that dimers are one of the first steps in the TD formation chain.

3.1.3 Dimer formation by electron irradiation

Studying defects like oxygen dimers and vacancy centers in Si with FTIR can be difficult because the IR bands are small and can be readily suppressed. Therefore, Si can be enriched with dimers by irradiation with high energy electrons [22]. From the radiation, self-interstitials and vacancies appear in

the material. This enhances the dimer formation when VO_2 centers, formed by irradiation at elevated temperatures, capture an interstitial silicon atom [22, 28]:

$$VO_2 + I \rightarrow O_{2\mathrm{i}}. \tag{3.2}$$

The concentration can now increase from 10^{14} cm^{-3} to about 10^{16} cm^{-3} and it is possible to detect the dimer peak in the absorption spectrum.

Watkins and Corbett [29, 30, 31] studied vacancy-oxygen centers with electron spin resonance and infrared absorption measurements using irradiated silicon samples. They found that a mobile vacancy can be trapped by an interstitial oxygen to make a vacancy-oxygen center (VO), also known as an A center,

$$V + O_{\mathrm{i}} \rightarrow VO. \tag{3.3}$$

The IR band from the VO center, at 830 cm^{-1} at RT, disappears at temperatures above 300°C and new IR bands appear. They presented a tentative model that suggests that at temperatures higher than 300°C, the VO centers trap interstitial oxygen to make VO_2 and VO_3 centers that give rise to new IR bands:

$$VO + O_{\mathrm{i}} \rightarrow VO_2 \tag{3.4}$$

and

$$VO_2 + O_{\mathrm{i}} \rightarrow VO_3. \tag{3.5}$$

At higher temperatures, they also suggested that the VO centers will decay,

$$VO + I \rightarrow O_{\mathrm{i}}. \tag{3.6}$$

Svensson et al. [32] suggested that dissociation and reforming of VO centers at temperatures above 300°C makes fast oxygen diffusion,

$$V + O_{\mathrm{i}} \rightarrow VO \tag{3.7}$$

and

$$VO + I \rightarrow O_{\mathrm{i}}. \tag{3.8}$$

The IR band appearing at 889 cm^{-1} originates from the free vacancies that encounter dimers in the lattice,

$$V + O_{2i} \rightarrow VO_2, \tag{3.9}$$

that results in VO_2 centers.

3.2 Other defects

3.2.1 Trimers

Trimers (O_{3i}) are formed by three interstitial oxygen atoms coming together [33, 34]. It begins with an oxygen dimer capturing an interstitial oxygen atom making a trimer,

$$O_{2i} + O_i \rightarrow O_{3i}. \tag{3.10}$$

and it gives rise to vibrational bands at 537, 723, 1006 and 1020 cm^{-1}.

Trimers can also arise from a mobile VO_2 that captures an O_i to make a VO_3 complex [16],

$$VO_2 + O_i \rightarrow VO_3, \tag{3.11}$$

for then capturing an interstitial Si atom to produce a trimer,

$$I + VO_3 \rightarrow O_{3i}. \tag{3.12}$$

3.2.2 Carbon

Carbon impurities in silicon crystals and its influences on the formation of TDs, have been widely studied. Carbon is found in substitutional sites in the crystal at high concentrations of about 10^{16} cm^{-3} and can form complexes with oxygen. It has been shown that these defects decrease TD formation [8, 14, 16, 19, 35]. Murin et al. [19] studied Cz-Si samples that were phosphorus and boron doped, whit a carbon concentration of $\leq$ 2x10^{16} cm^{-3}. They used FTIR to study the 1012 cm^{-1} band, in samples annealed at

temperatures where TDDs were formed, and found a reduction of the band in the samples containing high concentration of carbon. They concluded that carbon capture oxygen dimers and resulting in suppression of the TD formation.

The influence of carbon on ND formation is also widely discussed. High carbon content enhances the ND concentration by acting as a catalyst [15]. Another model suggests that carbon does not directly participate in the formation of ND and that an embryo with a not yet known nature is enhancing the ND formation [36]. Recently Singh et al. [16] stated that carbon and oxygen complexes do play an important role in ND formation at 650^{o}C and that carbon is enhancing the ND formation, not the embryos.

3.2.3 Hydrogen

The effect of hydrogen in Cz-Si on TDs has been widely studied. Stein and Hahn [37] introduced hydrogen to Cz-Si samples by a plasma. They used low-temperature IR absorption and spreading resistance probe measurements to determine the accelerated TD formation in the sample. They proposed that hydrogen has the role of a fast-diffuser to accelerate the formation of TDs in Cz-Si.

Murin et al. [38] studied formation kinetics of small oxygen clusters in hydrogenated samples. They used phosphorus doped Cz-Si and hydrogen was introduced to the crystal through heat treatment at 1200-1300^{o}C in H_2 ambient with a pressure of 1.0 and 1.5 atm. The samples were annealed isothermally in nitrogen ambient at different temperatures in the range of 280-370^{o}C. Employing FTIR, they concluded that hydrogen enhances the oxygen precipitation of small oxygen clusters like dimers and trimers.

3.2.4 Defects in boron-doped silicon

Defects due to boron doping have become an obstacle for silicon based solar cells. They enhance degradation of the solar cell under illumination. This effect is called light induced degradation (LID). The most popular model to explain this is the model where an immobile boron atom in a substitutional place (B_s), capture a mobile oxygen dimer and makes a B_sO_{2i} complex,

$$B_s + O_{2i} \rightarrow B_sO_{2i}. \tag{3.13}$$

This complex is believed to introduce energy states in the upper half of the band gap which act as recombination centers for holes and electrons. Coulomb attraction forces enhance the formation of the B_sO_{2i} complex because the oxygen dimer has a double positive charge, O_{2i}^{++}, and the substitutional boron atom is negatively charged, B_s^-, making a positively charged complex, $(B_sO_{2i})^+$ [26, 39, 40].

The model suggests that the formation of B_sO_{2i} has a linear and a quadratic dependence related to the boron and oxygen concentration, respectively [41]. It was recently found that the concentration of the boron-oxygen complex is not proportional to the boron concentration but the net doping, which is the boron-doping concentration minus the compensating doping (phosphorus doping) [42].

According to a new model, that also has gained some support recently, there is a boron atom in an interstitial place that is trapped by a dimer to form a B_iO_{2i} complex [43],

$$B_i + O_{2i} \rightarrow B_iO_{2i}. \tag{3.14}$$

Both models have some drawbacks and more investigations are still in progress. Based on the new model there is no explanation for the formation of interstitial boron atoms and also thermal stability. From recent research, the "old" model has an issue confirming that the formation is independent of the net doping, and also explaining the dimer diffusion [27].

A comparison between boron doped Cz-Si with samples that are aluminum, gallium or indium doped, shows that only boron doped silicon gives rise to LID in solar cells. It is proposed by Schmidt and Bothe that this occurs due to the smaller size of boron than aluminum, gallium and indium [26]. Beside all these issues, boron is the most desired and best doping element because of economical aspects [40].

Carbon has also shown a positive influence on the degradation of the solar cells. In boron doped silicon with a carbon concentration of $5x10^{16}$ cm^{-3}, the degradation is reduced by 30% [26].

Chapter 4

Experimental techniques and instrumentation

Theory on FTIR will be presented in this chapter which is based on the textbooks from Griffiths and de Haseth [7], Smith [44] and Shimura [2]. Sample information and experimental details will be provided as well.

4.1 Fourier transform infrared spectroscopy

IR spectroscopy is the study of how IR light interacts with matter. FTIR can be used for investigation of defects in silicon and is one of the best and most powerful IR techniques because of the Michelson interferometer that gives it some great advantages.

4.1.1 The Michelson interferometer

The Michelson interferometer was invented in 1880 by Albert Abraham Michelson and it was originally made for finding proof of the *luminiferous aether*, the medium that people at that time thought light was propagating through. For measuring wavelengths of light with the interferometer, Michelson got the Nobel Prize in Physics in 1907.

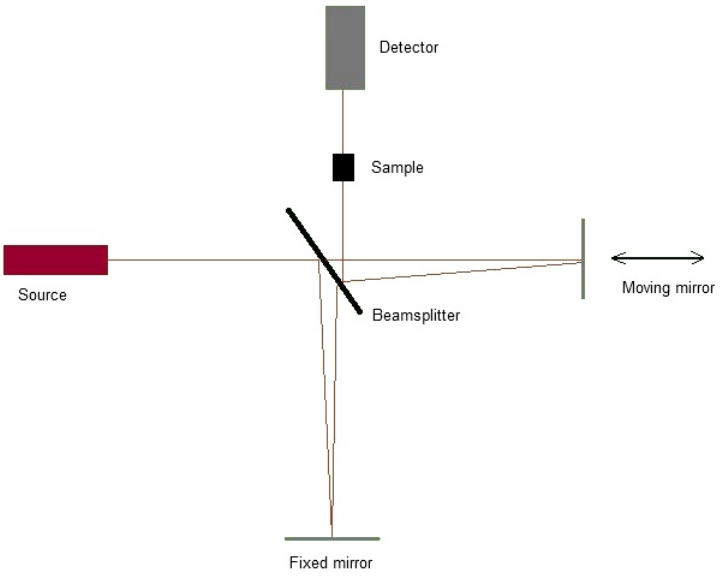

Figure 4.1: Schematic overview of the FTIR setup.

The Michelson interferometer consists of a beamsplitter, a moving and a stationary mirror that gives the posibility of measuring over all wavelengths in one scan. This is the advantage of FTIR compared to other IR spectroscopy techniques, that can only measure one wavelength at a time. A basic schematic overview of a FTIR setup is given in figure 4.1. A source radiates an infrared beam that is guided through the machine by mirrors. At the beamsplitter, the beam splits into two parts, one beam is directed to the stationary mirror and the other beam is directed to the moving mirror. The two beams are reflected by the mirrors and recombine at the beamsplitter, where they will interfere with each other constructively or destructively according to the path difference traveled by the two beams. The path difference is changed by the moving mirror. The difference in travel distance between the two beams is called optical path difference, δ. The relationship between mirror displacement, Δ, and δ is

$$\delta = 2\Delta. \tag{4.1}$$

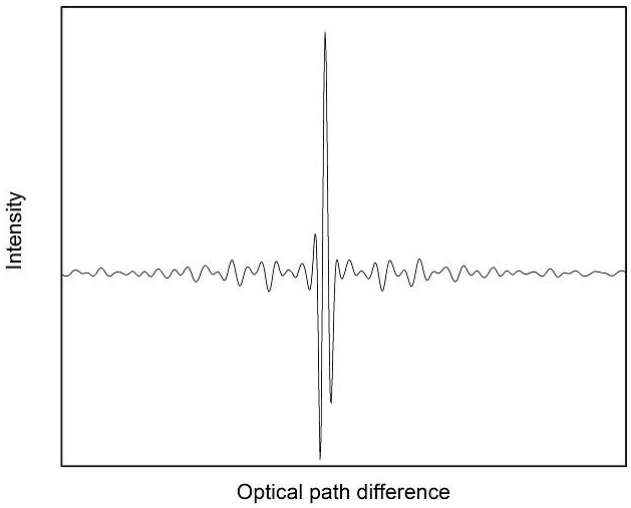

Figure 4.2: Interferogram: intensity versus optical path difference.

The mirror displacement needs to be multiplied with 2, because the beam will travel to the mirror and then back again, making the optical path difference twice the mirror displacement. As the mirror moves, the interference will shift from constructive to destructive, giving variation in the light intensity. This variation of light intensity with optical path difference is measured by a detector as a sinusoidal wave. An interferogram is produced when intensity versus optical path difference is plotted (figure 4.2). The interferogram contains all the sample information and is the basis for making an absorption spectrum.

4.1.2 Other components

One of the main components in FTIR is the infrared source. There are different types of sources based on the IR range to be measured. For the mid-infrared range, 400-4000 cm^{-1}, which is the range where dimers and TDs are studied, the most popular source is a resistively heated silicon carbide rod, also known as a Globar. For near- and far-infrared ranges, a quartz-tungsten-halogen (QTH) lamp and a high-pressure mercury lamp are used,

respectively.

There are not only different sources for different IR ranges, but also various beamsplitters and detectors. The potassium bromid (KBr) beamsplitter with a Ge coating is used in the mid-infrared range, while calcium fluorid (CaF_2) beamsplitter is used for 1250-15000 cm^{-1}.

When the IR beam has passed through the sample, it reaches the detector that converts it into an electrical signal. Detectors can be divided into two different types, thermal and quantum detectors. In the mid-infrared area the thermal detector is used and operates by sensing the changes in temperature of an absorbing material. The most popular one for investigating Si is a pyro electric bolometer called deuterated triglycine sulfate (DTGS). A quantum detector operates by exciting electrons to higher energy levels, when detecting IR radiation. Semiconductors are used as detectors in the mid- and near-infrared area. Mercury cadmium telluride (MCT) is a good detector for the mid-infrared range. It needs to be cooled to liquid nitrogen temperature to reduce noise which mainly arises from the sensitivity of the detector and noise from the leakage through the detector.

4.1.3 Advantages and limitations of FTIR

The best way to determine the performance of IR spectrometers is measuring the signal-to-noise ratio (SNR). SNR is determined by measuring the ratio of the height of an absorption peak in the spectrum and a level of noise on a nearby baseline point. The higher SNR, the better performance. If an absorption peak is less than three times as intense as the noise, the peak is most likely not real and is ignored.

FTIR has significantly higher SNR than other dispersive techniques because of two advantages. The first one is the high throughput (or Jacquinot), dispersive instruments mostly have slits that the light must pass and as a result the intensity decreases and restricts the wavenumber range of the in-

frared light, while in a FTIR instrument, all the light will reach the sample at the same time. The other advantage is the multiplex (or Fellgett) advantage, where all wavenumbers of the light are detected at once. Multiple scans can be added together and the relationship between SNR and number of scans added together, N, is

$$SNR \approx N^{1/2}. \tag{4.2}$$

One of the most important limitations of the FTIR technique is that it can not detect all substances, which do not have chemical bonds, do not make vibrational motion and do not absorb infrared radiation, like mono atomic ions or atoms.

Another limitation comes from FTIR being a single beam technique. The background spectrum must be measured at a different time than the sample. This leads to the possibility of a change in the environment that can result in water vapor or carbon dioxide peaks in the absorption spectrum.

4.1.4 LT and RT measurements

There are differences in RT and LT measurements by FTIR. RT is used for looking at the oxygen bands, but when it comes to study TDs and oxygen dimers, RT is not good enough. LT measurements are done by cooling the sample down to about 20 K or lower and this will result in decrease in vibrations between atoms. When the sample is radiated with IR light, more radiation can be absorbed and the peaks become high and sharp in the spectrum, compared to those at RT.

Defects that absorb radiation due to electronic transitions, like TDs, are often not visible at RT measurements. If defects make shallow donor states in the band gap, these states are empty at RT du to excitation of electrons. When the sample is cooled down, electrons return to the donor states and absorb IR light when irradiated and then become excited. This will result in absorption bands in the spectrum that are not visible at RT.

4.1.5 Fourier transform

To understand how the FTIR spectroscopy works, one needs to study Fourier transform which is used to calculate an IR spectrum from an interferogram. However, the classical Fourier transform is a very time consuming calculation and nowadays fast Fourier transform done on computers is mainly used.

Fourier transform is a mathematical operation where a signal as a function of time is transformed to a signal as a function of frequency. These are called the time and frequency domains of the signal.

An interferogram consists of a large number of sinusoidal waves added together, see figure 4.2. The most simple equation representing it is

$$S(\delta) = B(v_0) cos 2\pi v_0 \delta \tag{4.3}$$

where *S(δ)*, is the ac signal in volts from the amplifier, *B(v_0)* is the single-beam spectral intensity, v_0 is the wavenumber and δ is the optical path difference also called the retardation. *B(v_0)* gives the intensity of the source at wavenumber v_0, as modified by the instrumental characteristics.

When the source is a continuum, the interferogram and the spectrum can be regarded as a complex pair

$$S(\delta) = \int_{-\infty}^{+\infty} B(v) e^{i2\pi v\delta} dv \tag{4.4}$$

$$B(v) = \int_{-\infty}^{+\infty} S(\delta) e^{-i2\pi v\delta} d\delta \tag{4.5}$$

where *S(δ)* represents the interferogram and *B(v)* represents the spectrum. *S(δ)* is the complex inverse Fourier transform of the spectrum to produce the interferogram. The discrete Fourier transform of an interferogram of N points to produce a spectrum of n points may be written as

$$B(r) = \sum_{k=0}^{n-1} S_0(k) e^{-i2\pi rk/n} \quad r = 1, 2, ..., N-1 \tag{4.6}$$

where *B(r)* is the spectrum expressed at discrete wavenumbers r.

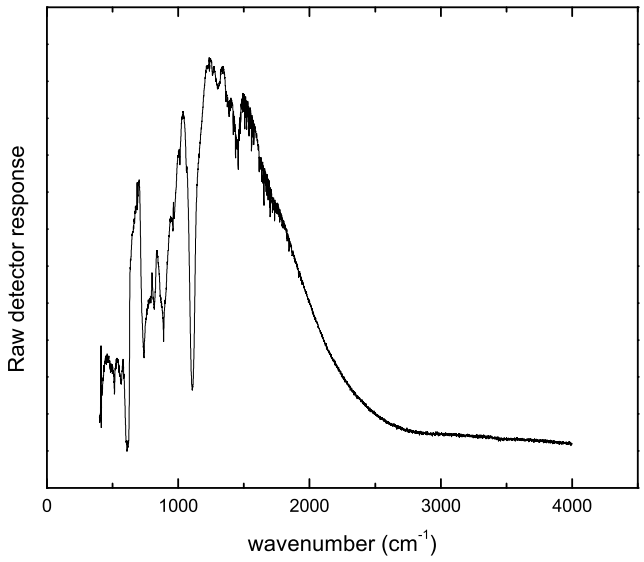

Figure 4.3: A single beam spectrum obtained after Fourier transformation of the interferogram.

4.1.6 Absorption spectrum

When the Fourier transform is done, a single beam spectrum is obtained, as shown in figure 4.3, which is a plot of raw detector response versus wavenumber. When measuring without a sample, but only the sample holder, a background spectrum is obtained. This spectrum gives the instrumental contribution (the instrument response function) and the environment contribution to the signal. A background spectrum is always measured first, so the contribution from the instrumental and the environment can be eliminated from the single beam spectrum. This produces a transmittance spectrum by

$$T = I/I_0 \tag{4.7}$$

where I is the intensity measured from the sample, the single beam spectrum, and I_0 is intensity measured from the background. The transmittance can

also be expressed by

$$T = e^{-A} \tag{4.8}$$

which shows how it relates to absorbance, A. An absorbance spectrum can be calculated from the transmittance spectrum by

$$A = -ln(T). \tag{4.9}$$

In order to obtain a good absorption spectrum from the impurities in silicon, an absorbance spectrum from a reference sample is made and is subtracted from the absorbance spectrum from the sample. The reference sample is Fz grown and has a substantially lower oxygen concentration than the Cz grown samples. Absorbance is unit less and to get absorption coefficient with unit cm^{-1} it is divided by the thickness of the sample.

4.1.7 Concentration measurements

FTIR can be used to find concentrations of species in silicon. By knowing the oxygen concentration in silicon, the oxygen precipitation, solubility, diffusion and interaction with other defects are easier to study. Also, knowing the oxygen concentration gives an understanding of the electrical, mechanical and optical properties of silicon.

The concentration of a specimen in the crystal is related to absorbance by Beer's law,

$$A = \epsilon \times l \times N \tag{4.10}$$

where A is absorbance, ϵ is absorptivity, l is path length and N is concentration. Hence, absorbance is proportional to the concentration of a component in the sample and changes with wavenumber.

The 1107 cm^{-1} band at RT is used for determining the O_i concentration. At LT several bands arise in the range of 1125-1140 cm^{-1}, where 1136.4 cm^{-1} is the highest peak and is an O_i related band. Other bands that are assigned to the O_i in the same range appear at 1129.2, 1132.7 and 1134.5 cm^{-1}. These

bands are quasimolecules of Si and O [45]. When it is difficult to determine the O_i concentration at RT, it can be done at LT by using the 1136 cm^{-1} band [46].

For determining the oxygen concentration employing the 1107 cm^{-1} band there are two methods using the integrated area, IA, of the peak and α, which is the amplitude of the peak. The concentration can then be found by multiplying with a calibration coefficient, c. The oxygen calibration coefficients for interstitial oxygen in silicon is $c_{IA} = 0,94 \times 10^{16}$ cm^{-1} [47], and $c_\alpha = 3.14 \times 10^{17}$ cm^{-2} [48].

For extracting interstitial oxygen concentration with IA,

$$N = IA \times c_{IA}. \tag{4.11}$$

For extracting with α, the concentration is given by

$$N = \alpha \times c_\alpha \tag{4.12}$$

where α is the height of the peak. These methods can also be used for calculating the dimer concentration from the 1012 cm^{-1} band. Then a ratio of the full width at half maximum, FWHM, between the dimer peak and O_i must be taken into account when using α,

$$N = \alpha \times (FWHM_{O2i}/FWHM_{Oi}) \times c_\alpha \tag{4.13}$$

For the IA method, the procedure is the same as for interstitial oxygen.

4.1.8 Activation energy

The activation energy, E_a, for a reaction is the energy barrier height which must be overcome in order to make the reaction happen. It can be expressed as an Arrhenius equation:

$$k = Ae^{-E_a/k_B t} \tag{4.14}$$

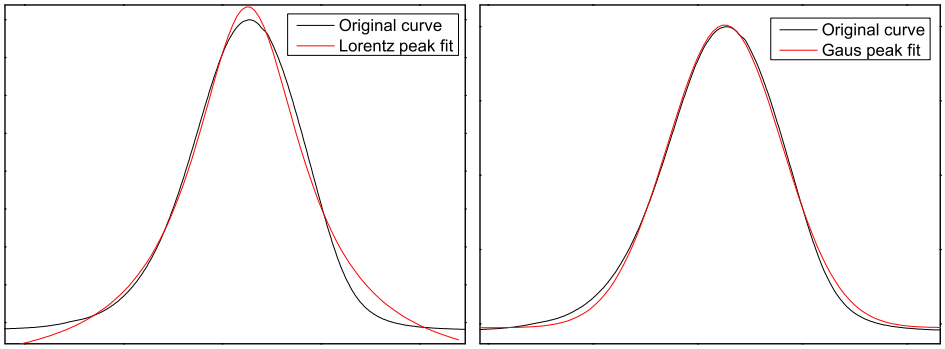

(a) Lorentz function (b) Gaus function

Figure 4.4: A bell shaped curve can be fitted with a Lorentz or a Gauss function.

where A is a pre-factor, k is the reaction rate, k_B is Boltzmann constant and t is the absolute temperature. The activation energy can be found by the slope of the Arrhenius plot, and A by the intercept with the y-axis.

4.1.9 Peak analyzing

To interpret all IR spectra, one needs to take into account the possibility of overlap from different peaks. In order to separate peaks a fitting process, that simulates peaks in the overlap area, can be used.

Two functions can be used to simulate a bell shaped curv: Gauss and Lorentz function, see figure 4.4. The Lorentz function is given by

$$y = y_0 + \frac{2A}{\pi}\frac{w}{4(x - x_c)^2 + w^2} \tag{4.15}$$

where A is the area, w is the width, x_c is the center and y_0 is the height of the peak. The Gauss function is given by

$$y = y_0 + \frac{A}{w\sqrt{\pi/2}} e^{-2\frac{(x-x_c)^2}{w^2}}. \tag{4.16}$$

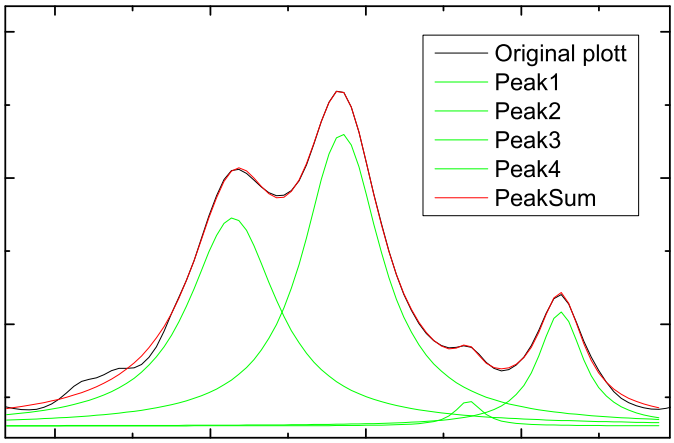

Figure 4.5: Multiple peak fit with the Lorentz function.

In the case of overlap, Lorentz or Gaussian functions for multiple peaks are used for fitting several peaks, see figure 4.5.

4.2 FTIR instrumentation at MiNa-Lab

The FTIR instrumentation used for measurements in this thesis is a Bruker IFS 113v infrared spectrometer and the interferometer is a Genzel interferometer. In this type of interferometer the beam is focused on the beamsplitter and its size is smaller than that of a Michelson interferometer.

An overview over the optical path of the IR beam is shown in figure 4.6. The IR beam is reflected and transmitted at the beamsplitter, and is lead by mirrors to the scanner. As the scanner moves, one of the path lengths increases and the other one decreases. For the Genzel interferometer the optical path difference is, therefore, 4 times the scanner displacement.

For LT measurements a Closed Cycle Helium CTI-Cryogenic Helix 22 Compressor 8200 was used to cool down the sample.

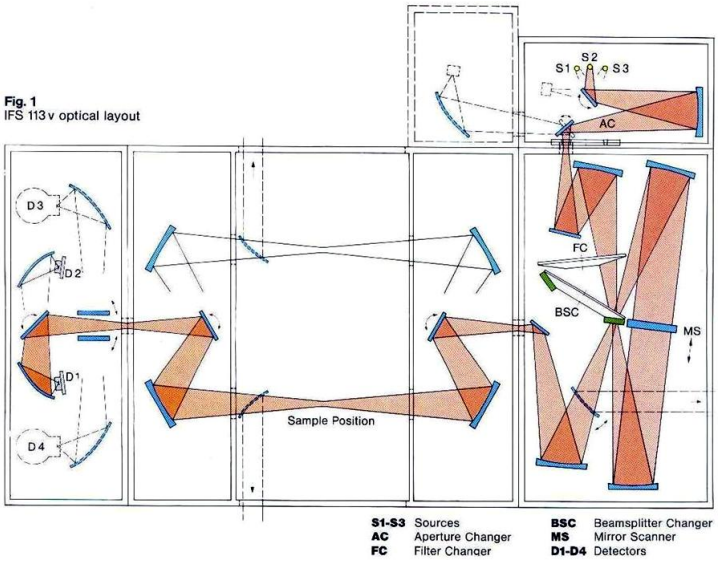

Figure 4.6: This picture is from the instrument booklet of the Bruker IFS 113v and shows an overview of the optical path of the IR beam. The scanner is a double sided moving mirror.

4.3 Four point probe method

The four point probe (FPP) method is used to measure electrical resistivity of a sample. The setup consists of four electrodes: two outer electrodes that is current-carrying and two inner electrodes that are voltage-sensing, see figure 4.7. The reason for four probes is to eliminate the influence of the resistance between the probes and the surface of the sample that must be taken in consideration when using a two probe method.

Voltage, V, and current, I, are measured and the resistivity, ρ, can be calculated by the equation

$$\rho = K(2\pi PV/I) \tag{4.17}$$

where K is a correction factor for the thickness of the sample ($K \to 1$ when measuring a thick sample) and P is the probe spacing.

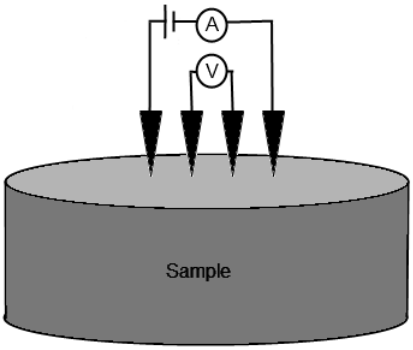

Figure 4.7: Four point probe measurement.

4.4 Sample details

The samples used in this thesis come from Siltronic AG at the Wacker group and are silicon mono-crystalline samples grown with the Cz pulling method. They have phosphorus doping making the material n-type, with a resistivity of about 50 Ωcm. They were polished to achieve optical surfaces on two sides and were irradiated with 2 MeV electrons at 320-350°C. The oxygen concentration is about 10^{18} atm/cm^3.

In table 4.1 the details of the samples are listed such as name, annealing temperature, and sample thickness. A400 and A350 have been annealed and measured in this study. The other samples have previously been measured and annealed by Thomas Hallberg and Leonid Murin, but the data have not been analyzed. These data will therefore also be interpreted in this thesis.

The reference sample used is a Fz grown Si sample with a thickness of 5.03 mm. The oxygen concentration is about 10^{16}atm/cm^3.

Sample	Sample thickness	Annealing temperature
A300	5.34 mm	300°C
A350	4.725 mm	350°C
A370	4.725 mm	370°C
A400	4.725 mm	400°C
A450	4.71 mm	450°C
A470	3.07 mm	470°C

Table 4.1: Sample overview

4.5 Experimental procedure

A DTGS detector, a Globar and a KBr beamsplitter were used in the FTIR measurement. In table 4.2 the annealing times and temperatures are presented with the sample name.

Sample	Annealing temperature, °C	Annealing times, h
A300	300	120, 240, 360, 480, 600, 2760
A350	350	2, 4, 8, 16, 32, 64, 128
A370	370	0.5, 1, 3, 5, 8, 28, 68, 164, 334
A400	400	0.5, 1, 2, 4, 8, 16, 32, 64
A450	450	0.1667, 1, 2, 4, 8, 16, 32, 60, 120
A470	470	1, 2, 3, 4

Table 4.2: Survey over the annealing times for each sample

FTIR measurements were done before annealing and after every annealing step. Annealing was done in a small furnace in air at constant temperatures. After each heat treatment, the samples were dipped in HF to remove the oxide layer that has been growing on the surface during annealing. Before each measurement they were cleaned in three steps with acetone,

ethanol and de-ionized water. The data were collected at RT and LT (20 K). FPP measurements were done on A400 and A350 after the last annealing step.

OPUS 3.0.17 [49] was used for extracting absorption spectra from the raw data and for baseline correction. Origin 8.1 [50] was used for analyzing the spectra, peak fitting and plotting.

For A400 and A350, the OPUS settings used in this thesis are listed in table 4.3. Setting 1 was used for A400 and setting 2 for A350.

OPUS settings

	Setting 1	**Setting 2**
Beamsplitter:	Kbr/Ge	Kbr/Ge
Detector:	DTGS	DTGS
IR-source:	SiC Globar	SiC Globar
Resolution:	1 cm^{-1}	1 cm^{-1}
Data range:	400-4000 cm^{-1}	400-4000 cm^{-1}
Aperture setting:	10 mm	10 mm
Sample scan times:	512	1500
Scanner velocity:	6.25 KHz	7.432KHz

Table 4.3: FTIR measurement settings for sample A400 (setting 1) and A350 (setting 2)

Chapter 5

Results and Discussion

This chapter begins with a discussion of the noise issues from the FTIR, followed by spectra, concentration calculations and FPP measurements.

5.1 Noise issues from FTIR

Figure 5.1 gives a closer look at the 1012 cm^{-1} dimer band at different annealing times of sample A400. It is difficult to interpret this spectrum because the level of noise is to high. By using different optical parameters when measuring the sample, like the number of sample scan times and scanner velocity, the noise level can be changed. A series of measurements were done with different numbers of sample scan times to find the best parameters for the lowest noise. Settings 1 and 2 in table 4.3 were used and the measurements were done at RT. Scan times of N = 1, 4, 16, 32, 64, 256, 512, 1024, 1500 and 2048 were measured. This was done by measuring two background spectra with the same sample scan time, which were then divided by each other to get the ratio, that shows how the noise varies along the spectrum. This is called 100% lines and in figure 5.2 a 100% line for the scanner velocity of 6.25 Hz is plotted. It shows an almost constant noise level in the area 850-1150 cm^{-1}.

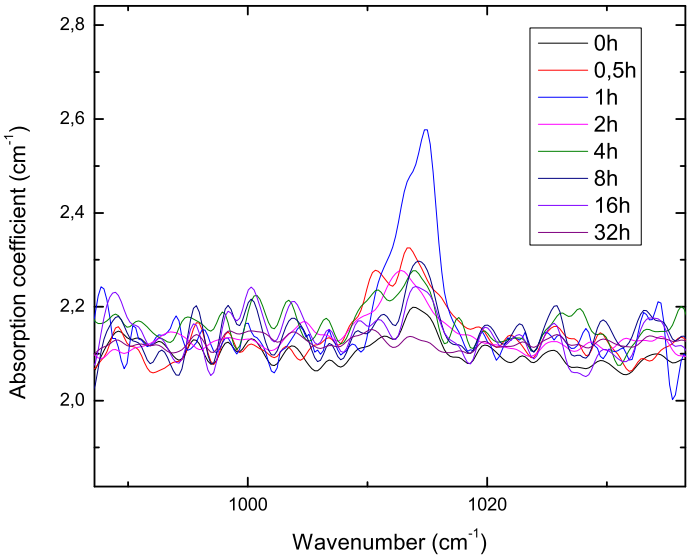

Figure 5.1: The 1012 cm^{-1} dimer band at RT with different annealing times for sample A400.

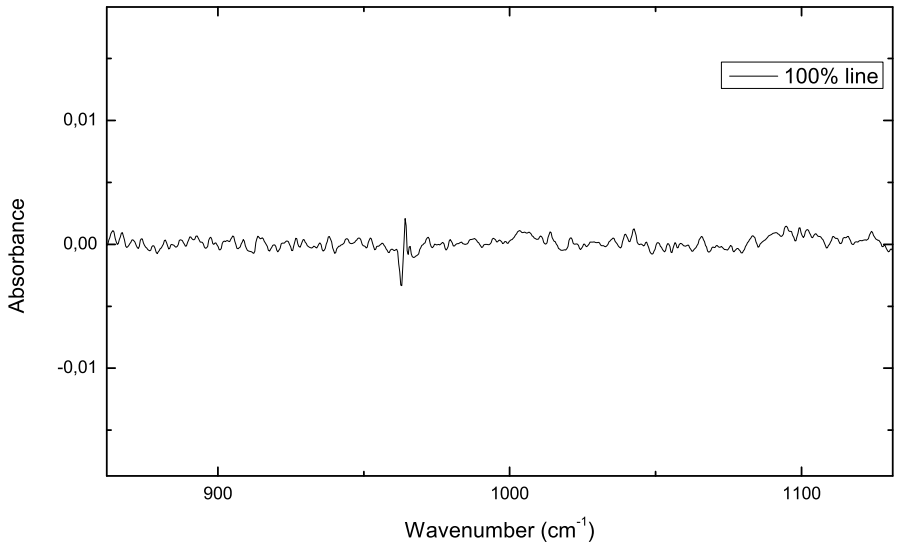

Figure 5.2: 100% line for sample scan time of 1500 with a scanner velocity of 6.25 Hz.

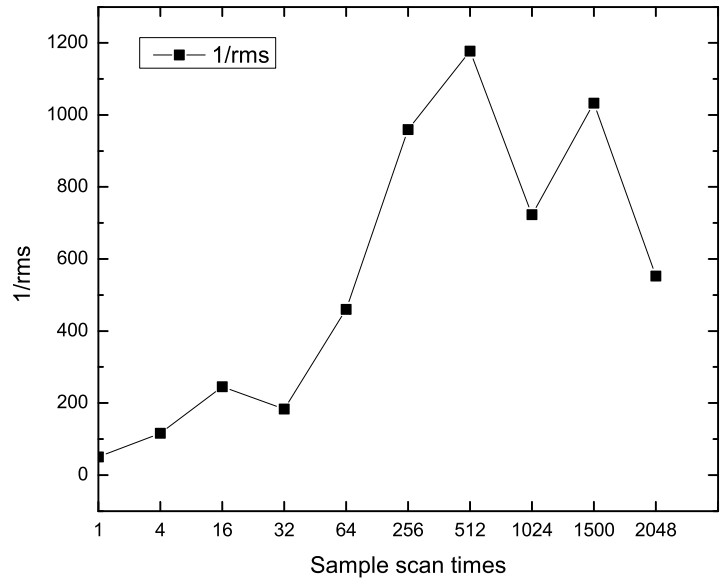

Figure 5.3: Reciprocal rms values at 6.25 Hz.

The rms noise, $x_{rms,}$ is the standard deviation of N data points in one area and can be calculated by

$$x_{rms} = \sqrt{\frac{1}{n}\sum_{i=1}^{n} x_i^2}. \tag{5.1}$$

The area of interest is at 900-1100 cm^{-1}. The inverse standard deviation values were plotted with sample scan time, see figure 5.3, and the best sample scan time that gave the lowest noise was found to be 512.

For a scanner velocity of 7.432 Hz, only 512, 1024 and 1500 sample scan times were measured to compare with the rms values from 6.25 Hz, see figure 5.4, which shows that the best sample scan time with the lowest noise was at 1500, and that a scanner velocity of 7.432 Hz gives a lower noise than 6.25 Hz. From this, 512 and 1500 sample scan times will be used for 6.25 and 7.432 Hz, respectively.

Another possible reason for the high level of noise is called *Zachory-*

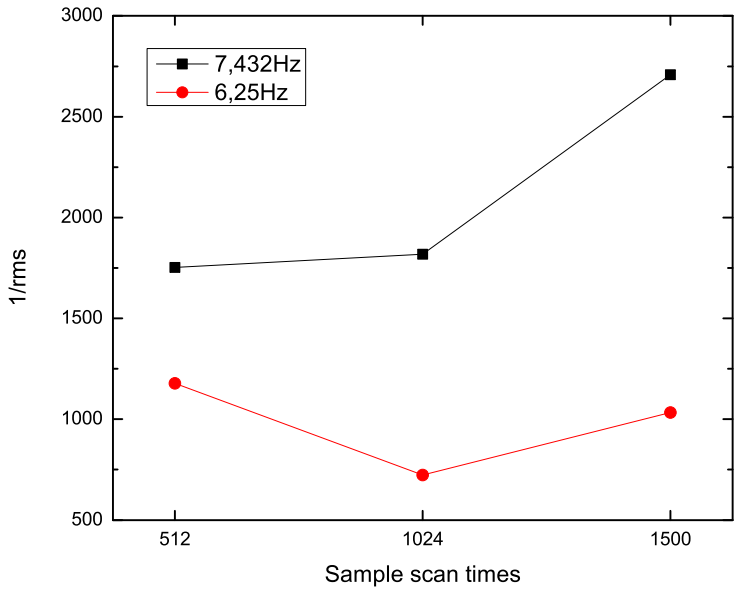

Figure 5.4: Rms at 6.25 Hz and 7.432 Hz.

Aaronson noise [7], which appears when the velocity of the optical scanner is not precisely constant. The FTIR had issues with the optical scanner changing frequency and stopping which affected the results, as seen in figure 5.5. The figure shows large changes in rms values, that come from the broken scanner changing frequency.

After repair, the noise level decreased. Figure 5.6 gives an overview over absorption spectra measured from A350, before and after the FTIR was repaired. There is a big difference in the noise level and after the repair it decreased for both LT and RT. From this it seems that the noise problem came from the broken scanner. The optical parameters extracted from the 100% lines and rms values were measured after the repair, so the broken scanner was not affecting these results.

Also, it can be seen that the peaks amplitude, in figure 5.6, is higher before repair than after, at LT measurements, which means that there are

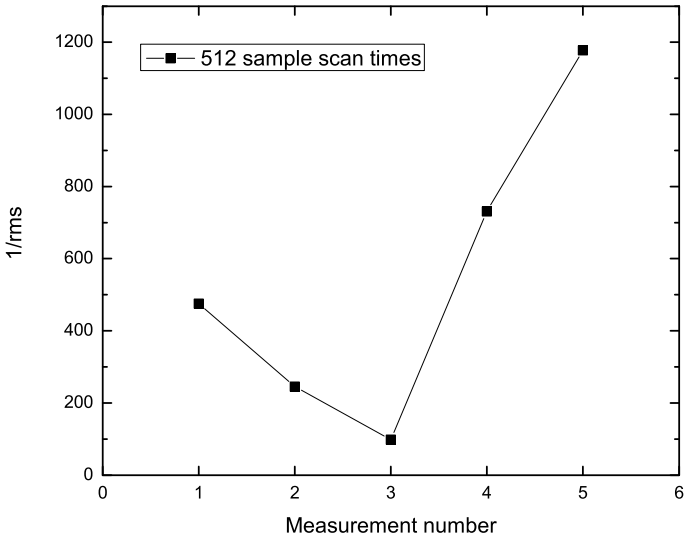

Figure 5.5: The measurements of 512 sample scan times were done five times and the rms plotted. The rms values change significantly.

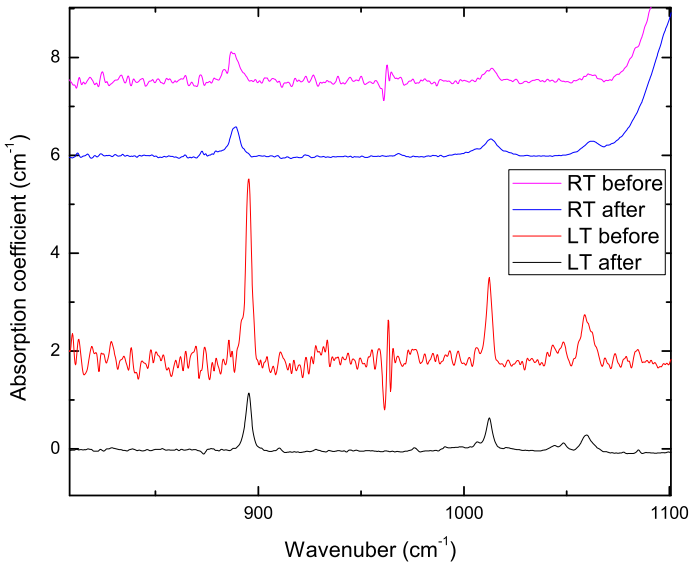

Figure 5.6: Absorption spectra from A350 comparing the noise before and after the FTIR was repaired.

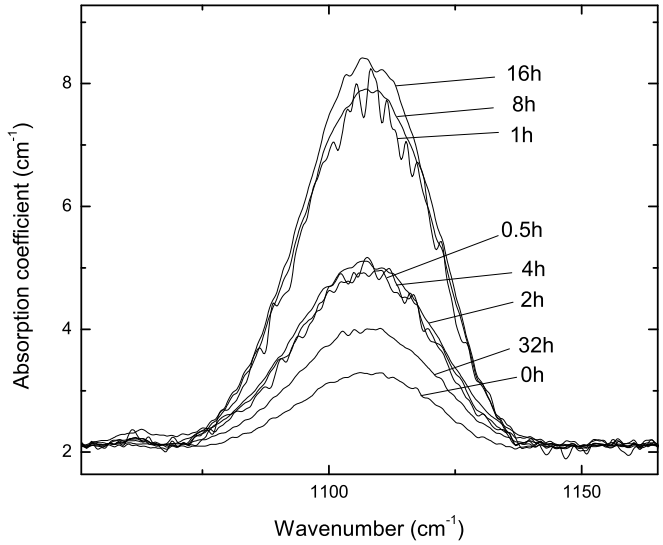

Figure 5.7: The oxygen 1107 cm^{-1} band at RT with different annealing times for sample A400.

other issues than only the noise, but also change in amplitude of absorption peaks. This can be seen in figure 5.7, where the 1107 cm^{-1} oxygen band at different annealing times at RT is plotted for sample A400. Comparing this band with the same band from sample A450, see figure 5.12, that was measured at a time when the FTIR worked perfectly, shows that the change in amplitude is slowly decreasing slightly and not behaving as seen in sample A400. Each measurement on A400 was done in equal conditions and with the same optical setting (setting 1). Sample A350 was measured after the repair and the 1107 cm^{-1} oxygen band at different annealing times at RT is given in figure 5.8. The same issue found in A400 is appearing in A350. One reason can come from the FTIR still not working correctly. Another reason can come from the mounting of the sample. The oxygen concentration in the Si samples is not homogeneous, which makes it important to mount the sample on the sample holder exactly at the same place for each measurement.

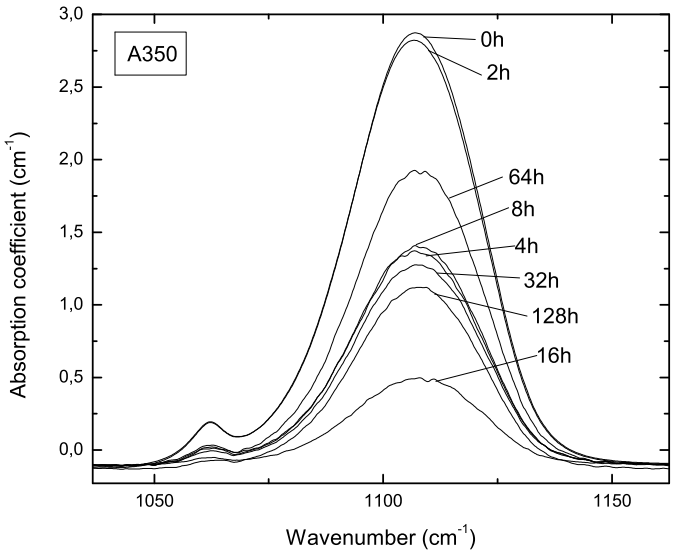

Figure 5.8: Large changes in amplitude are also seen for sample A350.

These issues must be taken into consideration when looking for patterns in the dimer concentration, which can seem enhanced, when in reality it is stable or decreasing. Due to these issues, the results from sample A400 and A350 were not used in the dimer concentration calculations.

5.2 As-grown and after irradiation

As-grown samples have a small dimer concentration of about 10^{14} cm^{-3}, and to be able to see the dimer peaks in the IR-spectrum, the samples were irradiated at elevated temperature (∼300°C) with high energy (2 MeV) electrons to doses in the 10^{18} cm^{-2} range. Figure 5.9 shows a plot of the oxygen and the dimer bands at RT for an as-grown sample and after irradiation. The dimer bands at 1012 cm^{-1} and 1060 cm^{-1} have increased and come from vacancies and interstitials that appear in the sample after irradiation. Also, a reduction in the interstitial oxygen band at 1107 cm^{-1} can be seen, which

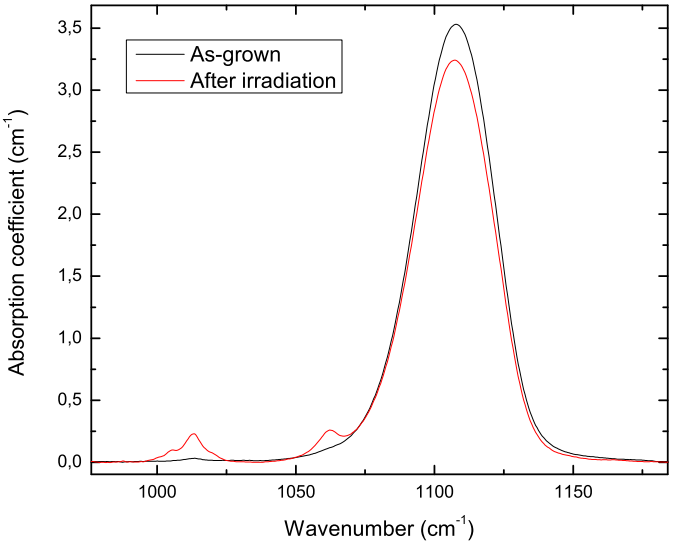

Figure 5.9: As-grown and irradiated IR-bands from sample A370 at RT.

comes from two O_i atoms forming a dimer.

Figure 5.10 gives a closer look at the 1012 cm^{-1} dimer band of sample A370 and shows the difference in amplitude of as-grown and irradiated sample. Also, a small band at 1006 cm^{-1} can be seen. This band is assigned to the oxygen trimer [33].

An overview of bands appearing at LT measurements of sample A400, measured after irradiation, is given in figure 5.11. Dimer peaks at 1012 and 1060 cm^{-1} can be seen, as well as a VO_2 center at 895 cm^{-1}.

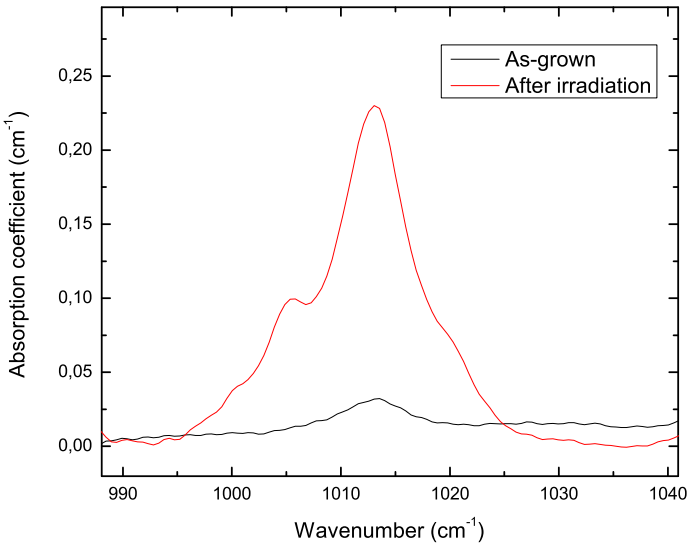

Figure 5.10: A closer look at the 1012 cm^{-1} dimer band from as-grown and after irradiation spectra of A370.

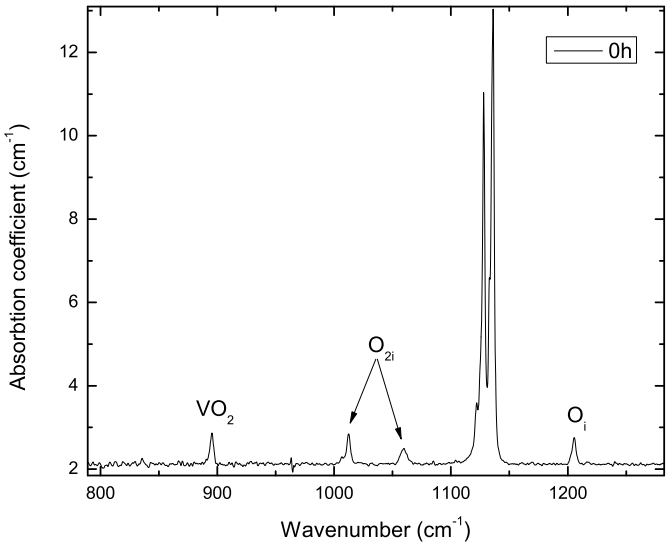

Figure 5.11: IR spectrum of A400 before annealing.

5.3 Oxygen bands

To study interstitial oxygen, RT measurements are used. In figure 5.12 the O_i band at 1107 cm^{-1} for sample A450 can be seen. The band shows a decreasing trend as the annealing time increases. This comes from the interstitial oxygen making complexes in the material like VO_3 centers. This will be further discussed in the VO_x section further down. The 1060 cm^{-1} dimer band can also be seen, which decreases with increasing annealing time.

Figure 5.13 gives an overview of the interstitial oxygen bands that appear at LT for sample A300. The figure shows the different Si-O stretching bands that appear from 1075 to 1220 cm^{-1}.

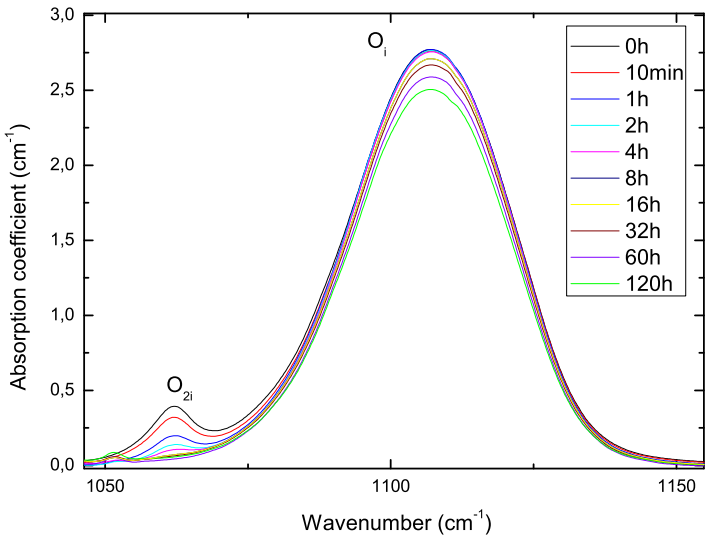

Figure 5.12: RT measurements from sample A450 showing the interstitial oxygen band at 1107 cm^{-1}at different annealing times.

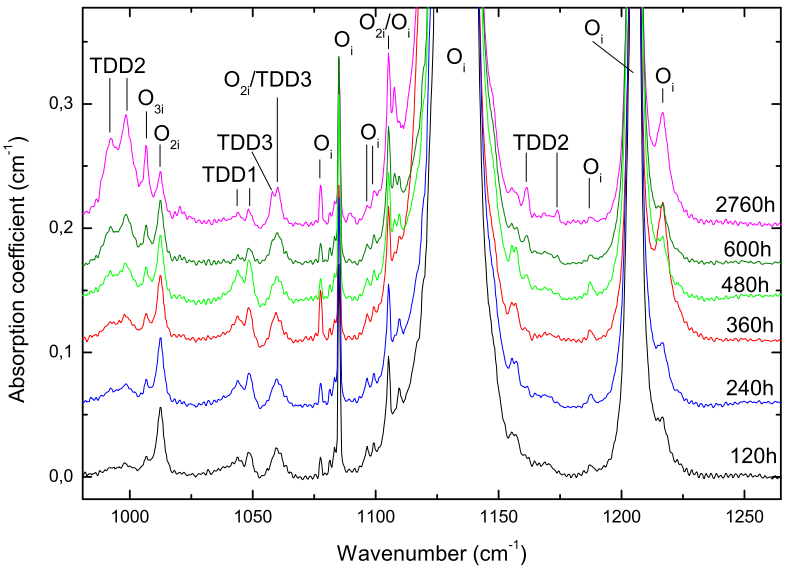

Figure 5.13: LT measurement overview of sample A300.

5.4 Dimers

The difference between RT and LT measurement is given in figure 5.14, showing dimer bands at 1060 and 1012 cm^{-1}. At LT they are higher and more narrow than at RT, and the 1060 cm^{-1} band does not overlap with the oxygen band at 1107 cm^{-1}. This shows that LT measurements are preferable for studying dimer bands.

Figure 5.15 gives an indication of how the 1012 cm^{-1} dimer band changes with annealing time for sample A370 at LT. It decreases with annealing time due to dissociation into TDDs. More 1012 cm^{-1} dimer band spectra can be found in appendix A.1.

In figure 5.16 the 556 cm^{-1} dimer band is shown for sample A370 at LT. The peak decreases in amplitude with increasing annealing time, which is the same as seen for the 1012 cm^{-1} band. In figure 5.17, the amplitude of the dimer band at 556 cm^{-1} versus annealing time is plotted and shows an exponential dependency on the annealing time. Other samples where the 556 cm^{-1} band could be seen were samples A450 and A470, see figure 5.18. Also, the amplitude of A450 at RT show an exponential dependency on the annealing time.

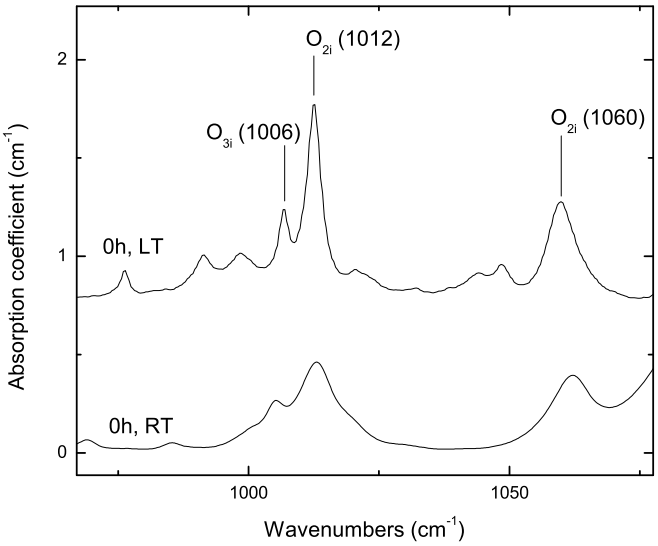

Figure 5.14: Difference in dimer bands of RT and LT measurements, after irradiation of sample A450.

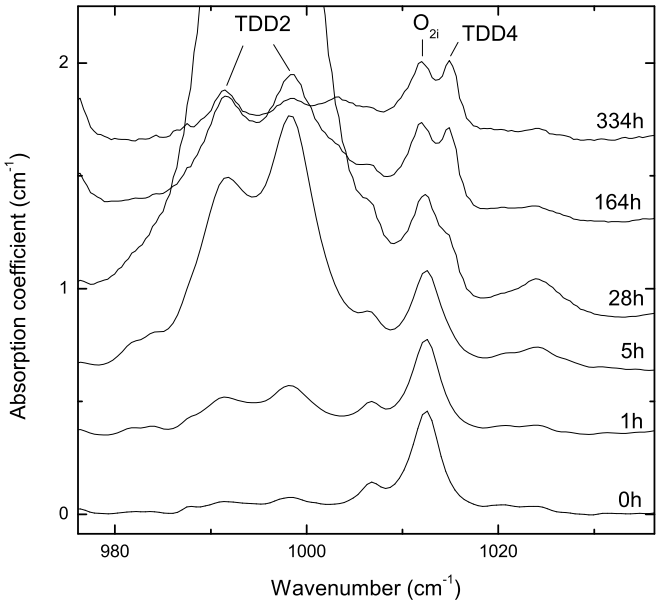

Figure 5.15: The development of the 1012 cm^{-1} dimer band at increasing annealing time for sample A370 at LT.

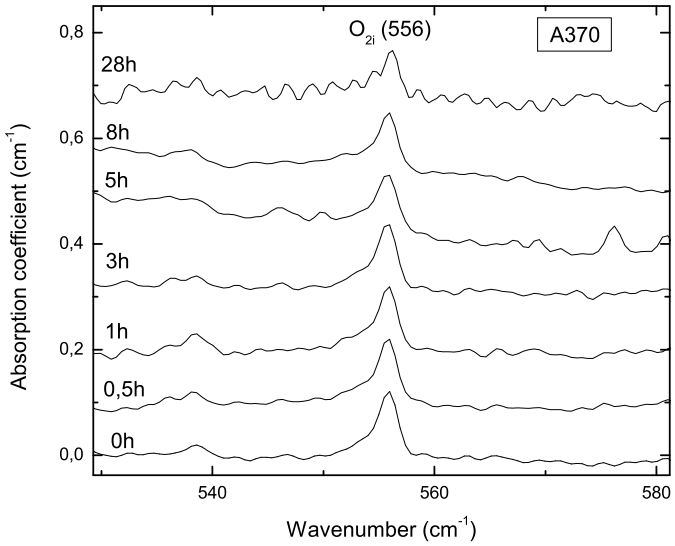

Figure 5.16: The 556 cm^{-1} dimer band at LT, show a decreasing trend in amplitude with increasing annealing time for sample A370.

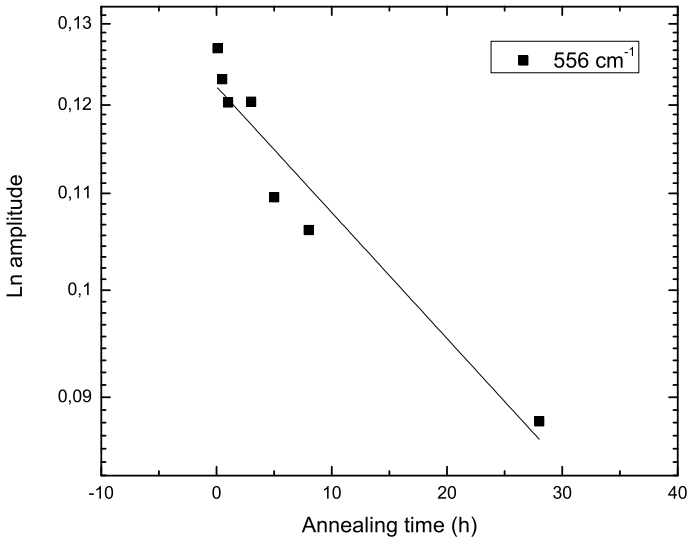

Figure 5.17: Amplitude versus annealing time for 556 cm^{-1} dimer band in sample A370 at LT.

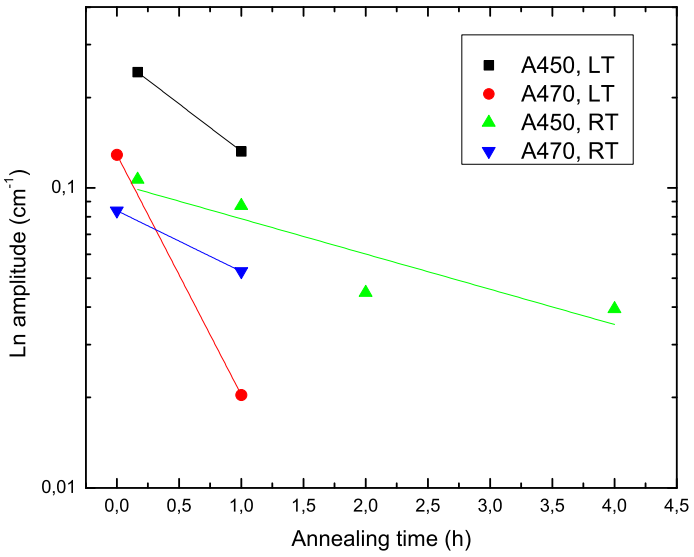

Figure 5.18: Change in amplitude of the 556 cm^{-1} band for samples A450 and A470.

5.5 TDDs

Comparing RT and LT measurements, as shown in figure 5.19, it is clear that TDD bands only appear at LT. This is due to the electronic transition bands of the TDDs. At RT the TDD states are empty and no energy can be absorbed, but at LT they are filled and electrons can be excited to the conduction band when radiated with IR light. Therefore, LT measurements are used for studying TDDs. Also, due to the electronic transition bands, the peaks in the spectra become larger than peaks from vibrational bands. It is important to take this into consideration when studying bands in a spectrum, and it also makes it more difficult to investigate TDD concentrations.

Figure 5.20 gives an overview of bands that appear in A370 at LT measurements from about 600-1100 cm^{-1}. The TDDs range from TDD2 to

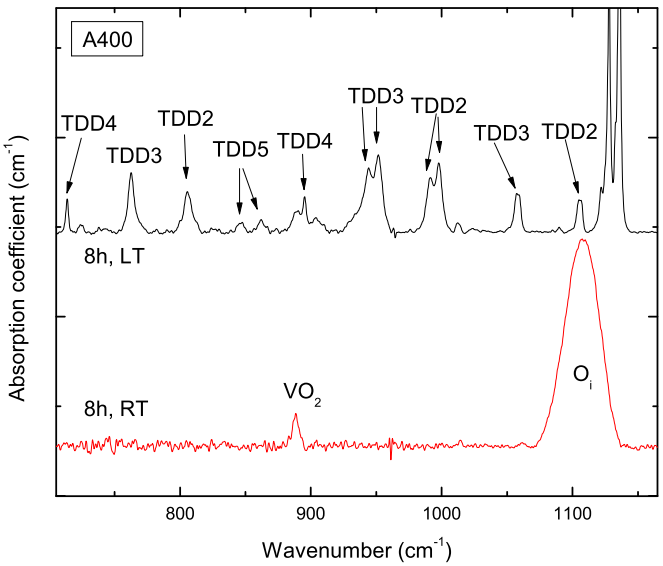

Figure 5.19: RT and LT measurements after 8h of annealing for sample A400. TDD bands can not be seen at RT only at LT.

TDD6 and appear after only 0.5 h annealing at 370°C. Figure 5.21 gives an overview of the bands that appear in A450 at around 600-1200 cm^{-1} for different annealing times. TDDs start to appear after only 10 minutes annealing at 450°C.

Looking at the overviews of the different samples, it is seen that TDDs appear faster in samples annealed with higher temperatures. This indicates that the time it takes for the TDDs to show up in a sample decreases with increasing annealing temperature, because more energy and higher temperatures will make the reaction go faster.

The dimer bands decrease and the TDD bands increase with annealing time. Dimers have vibrational bands and TDDs have electronic transition bands, which is why the TDDs bands are larger than the dimer bands at LT. Dimers are believed to evolve into TDDs [19] at temperatures around 300-500°C, which is explained by the decreasing dimer concentration as TDD

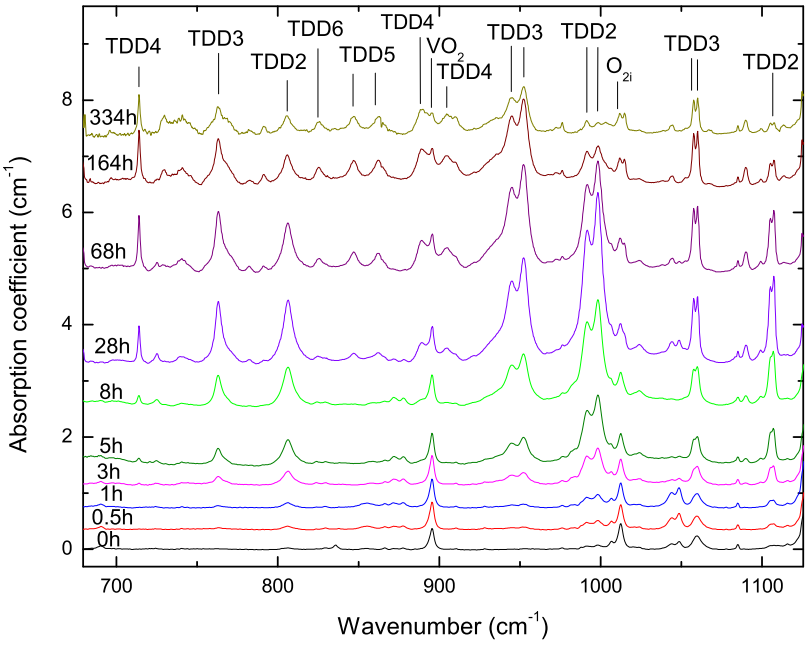

Figure 5.20: Overview of LT measurements for A370 annealed at 370°C.

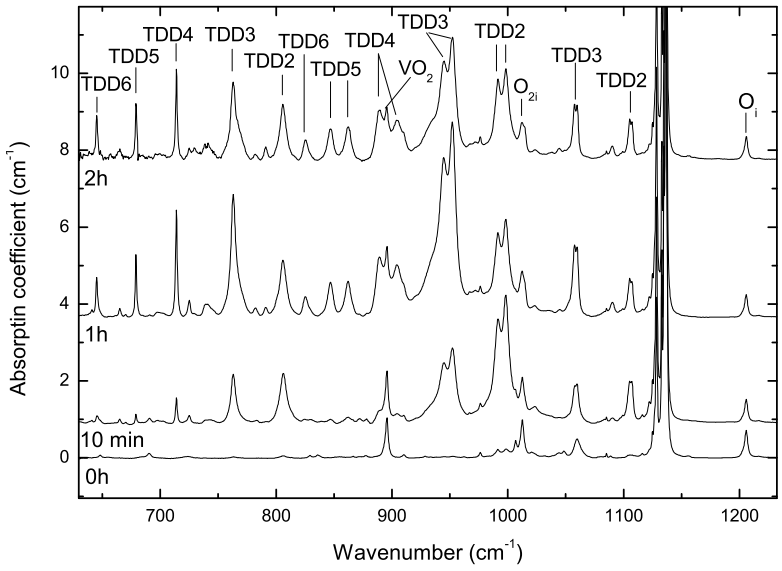

Figure 5.21: Overview of TDD bands appearing for A450 at LT measurements.

concentrations increase. After extended annealing, the TDD bands start to decrease, which happens earlier at higher annealing temperatures. This decreasing trend comes from TDDs getting annihilated [13]. A decrease in the TDD concentration after extended annealing at 450°C has been seen by Wijarabakula [51].

5.6 VO_x centers

In figures 5.22 and 5.23 an overview of VO_x bands for A370 and A470 is given, respectively. The peak at 889 cm^{-1} is the VO_2 center [31]. The 905, 969 and 1001 cm^{-1} bands are assigned to the VO_3 center [34]. There also seems to be a small VO_4 band at 986 cm^{-1} [22]. The VO_2 center decreases with annealing time, while VO_3 and VO_4 centers increase. Svensson et al. [52], who studied VO_x centers under heat treatment, suggested that this decay comes from VO_2 centers trapping a diffusing oxygen interstitial to form a VO_3 center. Later, Lindström et al. [53] suggested that the VO_2 center also could diffuse by changing to a bistable configuration, and forming a VO_3 center with an interstitial oxygen.

The figures in 5.24 show how VO_2 and VO_3 centers change in amplitude with annealing time for samples A370 and A450. Figure 5.25 shows loss of VO_2 versus growth of VO_3 for sample A450. The relationship is linear which indicates that VO_3 centers appear from VO_2 centers.

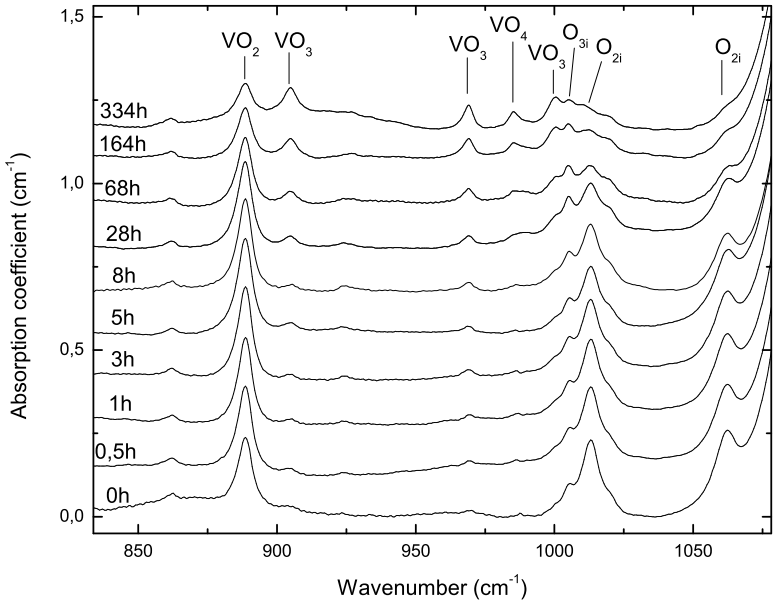

Figure 5.22: RT measurements of sample A370 showing VO_x bands.

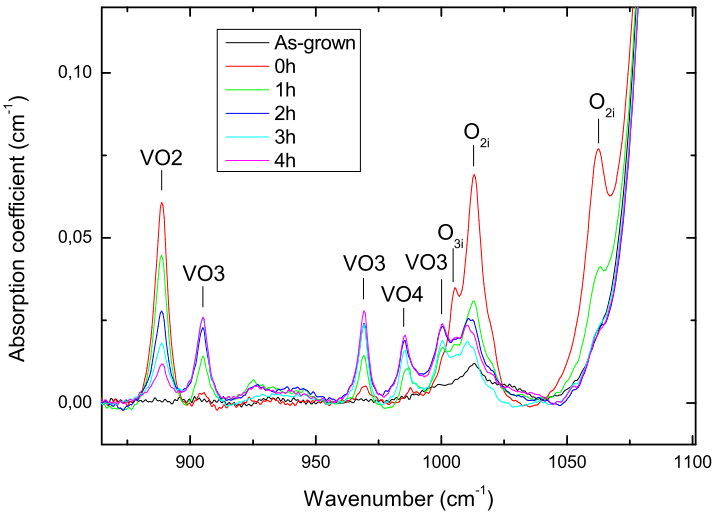

Figure 5.23: RT measurements of sample A470 showing VO_x bands.

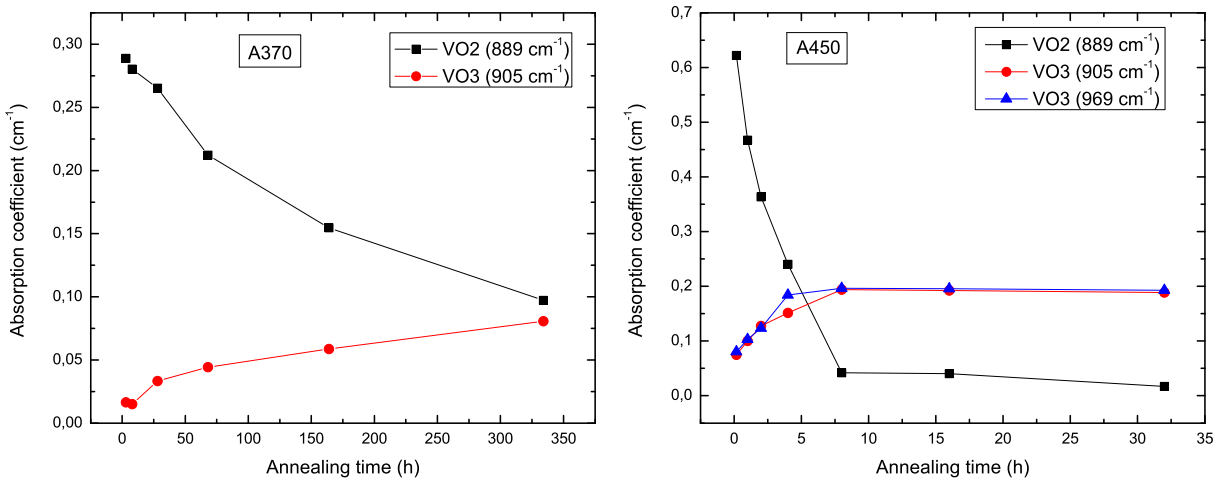

(a) A370 (b) A450

Figure 5.24: Change in amplitude for the VO_2 and VO_3 centers with annealing time at RT measurements.

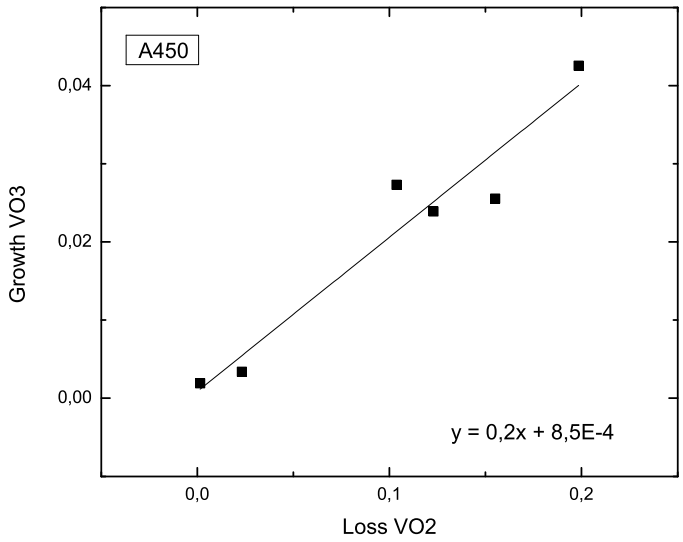

Figure 5.25: Growth of VO_3 versus loss of VO_2 in sample A450.

5.7 Concentration calculations

In this section the concentration calculations that were done on O_i and dimer bands will be presented with activation energy calculation from the decreasing dimer band.

5.7.1 Modeling bands with overlap

Extracting IA and α from peaks, which are overlapped by other peaks, can be difficult. By using a modeling function as described in section "Peak anayzing" (4.1.9) in chapter "Experimental techniques and instrumentation", peaks can be differentiated. This can be done by hand, which is time consuming and demands high accuracy, or the modeling can be done by a computer using a program like Origin.

When calculating dimer concentrations from low temperature measurements it is important to take the TDD4 band at 1014.6 cm^{-1} and TDD2 bands at 991.7 and 998.2 cm^{-1} into consideration. These bands overlap with the dimer band at 1012 cm^{-1} when measuring at LT, see figure 5.26. When calculating the dimer concentration the results can be affected by overlap and the concentration can seem larger than it is. There is also overlap from the trimer band at 1006 cm^{-1}.

5.7.2 Interstitial oxygen concentration

The O_i concentration is extracted using the 1107 cm^{-1} band, measured at RT. In table 5.1 values from after irradiation are given. The solubility of oxygen in silicon is about 2×10^{18} cm^{-3} [54] which gives an indication of the values expected. The calculated concentrations are plotted with annealing time to show what happens with the interstitial oxygen concentration when samples are annealed, see figure 5.27, 5.28, 5.29 and 5.30. For sample A300 the oxygen concentration seems to be stable, and for A370, A450 and A470

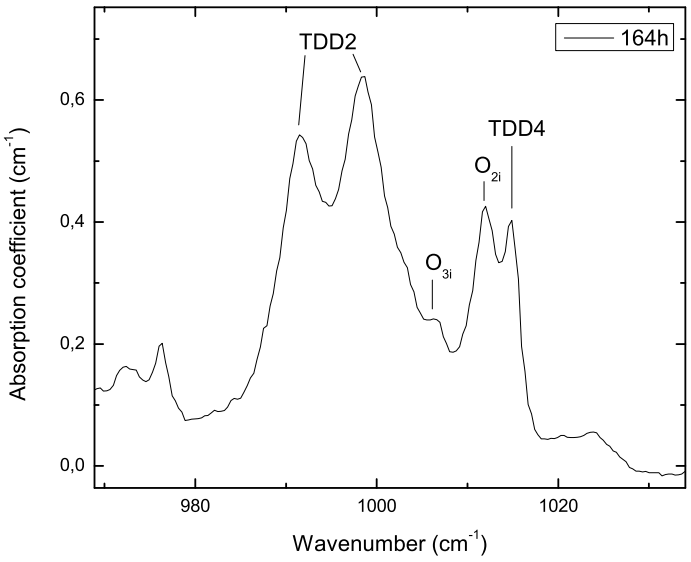

Figure 5.26: Overlap after 164 h annealing for sample A370.

it decreases with annealing time. The decrease in interstitial oxygen concentration can come from oxygen atoms making complexes with TDDs or VO_2 centers, as already discussed.

Sample A300 has a more stable concentration of oxygen than the other samples, which can come from the low annealing temperature at 300°C. Figure 5.31 shows an overview of bands appearing at RT for sample A300. Interstitial oxygen and dimer bands can be seen, and the VO_2 bands seem to be suppressed, which means that it is a small concentration of VO_2 centers in the material. This comes most likely from the irradiation of the sample, where V and I are formed. When the concentration of VO_2 is small, the concentrations of VO_3 and VO_4 centers, also should be small, since they are formed by VO_2 centers and an O_i. This can be seen in the spectrum by a lack of VO_3 and VO_4 bands and a non decreasing O_i band.

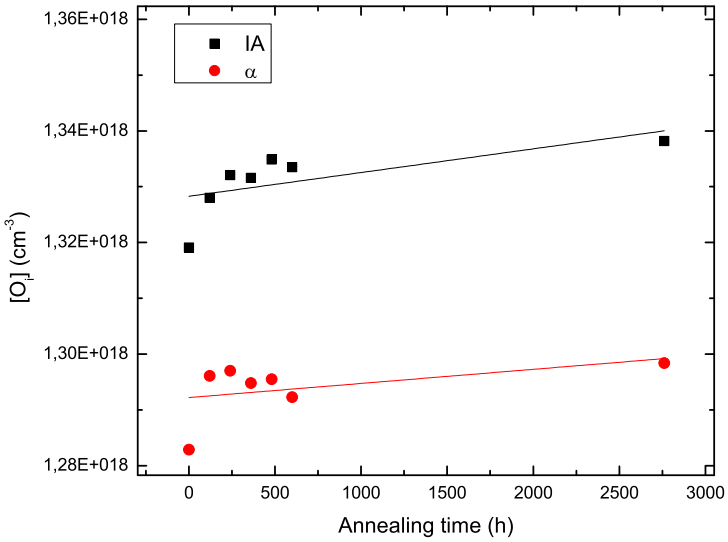

Figure 5.27: Interstitial oxygen concentration versus annealing time for sample A300 extracted by IA and α.

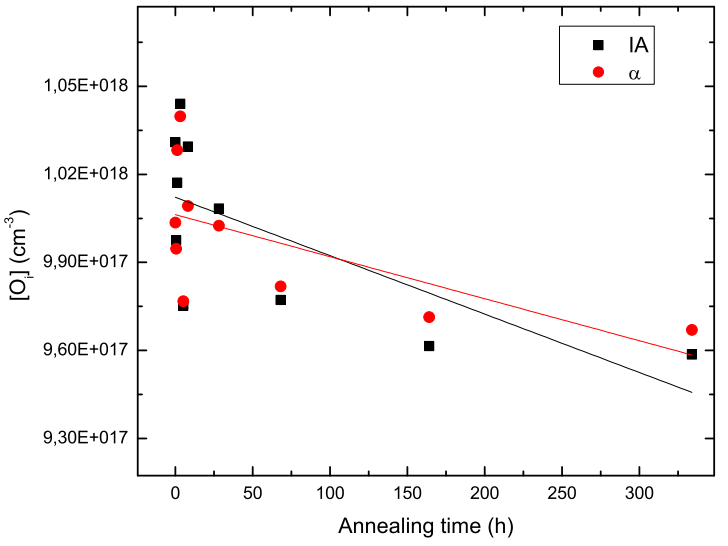

Figure 5.28: Interstitial oxygen concentration versus annealing time for sample A370 extracted by IA and α.

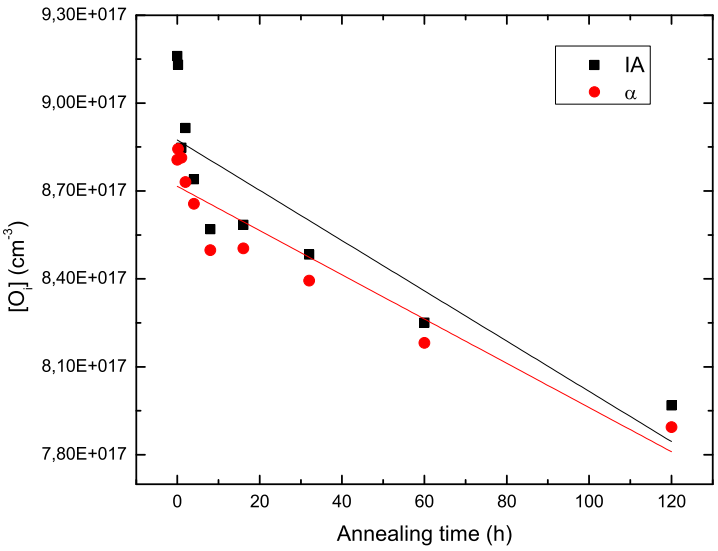

Figure 5.29: Interstitial oxygen concentration versus annealing time for sample A450 extracted by IA and α.

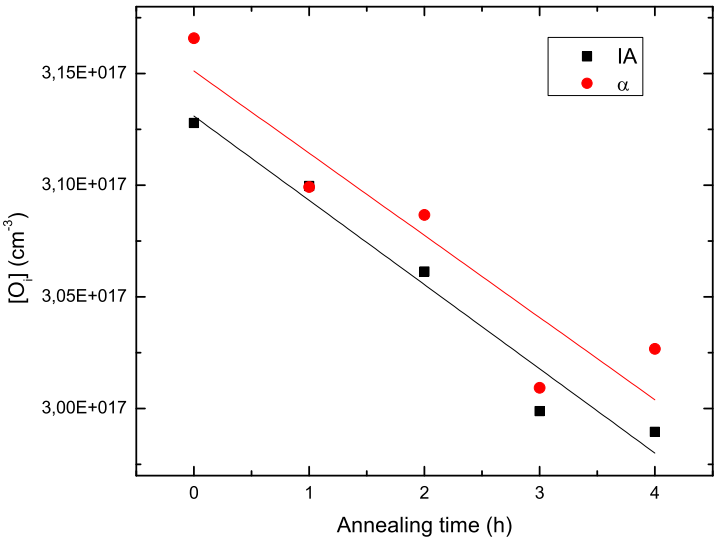

Figure 5.30: Interstitial oxygen concentration versus annealing time for sample A470 extracted by IA and α.

Sample	$[O_i]$ (cm^{-3})	
	IA	α
A300	$1{,}32\times10^{18}$	$1{,}28\times10^{18}$
A350	$9{,}55\times10^{17}$	$9{,}49\times10^{17}$
A370	$1{,}03\times10^{18}$	$1{,}00\times10^{18}$
A400	$3{,}70\times10^{17}$	$3{,}91\times10^{17}$
A450	$9{,}16\times10^{17}$	$8{,}81\times10^{17}$
A470	$3{,}13\times10^{17}$	$3{,}17\times10^{17}$

Table 5.1: O_i concentrations extracted by IA and α, from the 1107 cm^{-1} band, after irradiation.

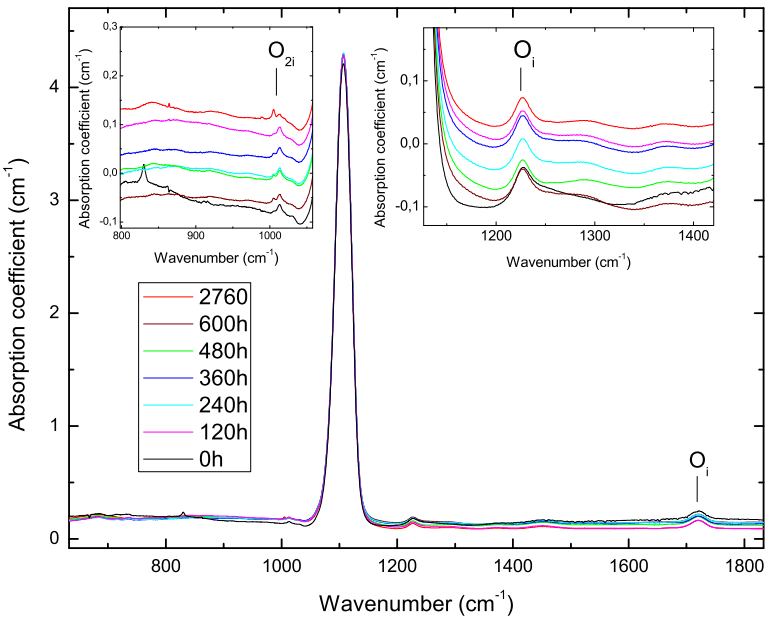

Figure 5.31: An overview of bands appearing at RT for sample A300.

5.7.3 Dimer concentration and activation energy

Dimer concentrations were extracted from the 1012 cm^{-1} dimer band and plotted with annealing time, see figures 5.32, 5.33, 5.34 and 5.35, that show how the dimer concentration decreases with annealing time. The concentration can be described by an exponential dependence with annealing time, which suggest that the reaction follows first order kinetics.

The dimer concentrations extracted by IA and α, before annealing, were found to range from 2.6×10^{15}-4.6×10^{16} cm^{-3} and 1.1×10^{15}-3.5×10^{16} cm^{-3}, respectively. From this it can be seen that the concentrations extracted by using α are lower than with IA. The reason for this is that the concentration extracted by α is dependent on the amplitude (α) and the FWHM, which can experience more changes in values when using different functions to model peaks than IA, which is the integrated area of the peak. The two methods have shown to give the same values for dimer diffusion activation energies, see table 5.2, and therefore they are both evenly good for this purpose.

It is not fully clear what happens when the dimer concentration decrease in the sample. Since the reaction follow first order kinetics, as shown above, the reaction rate is given as

$$-\frac{d[O_{2i}]}{dt} = c_1[O_{2i}], \tag{5.2}$$

where c_1 is the reaction rate constant and $[O_{2i}]$ is the dimer concentration. The activation energy, E_a, is given by

$$c_1 = c_0 e^{-E_a/k_B t}, \tag{5.3}$$

where c_0 is a frequency factor. c_1 can be found from

$$[O_{2i}] = [O_{2i}](t=0)e^{-c_1 t}, \tag{5.4}$$

which were found from the slope of the dimer concentration plots. Plotting c_1 with reciprocal temperature, see figure 5.36, gives E_a from the slope and c_0 from the intersect at the y-axis, see table 5.2.

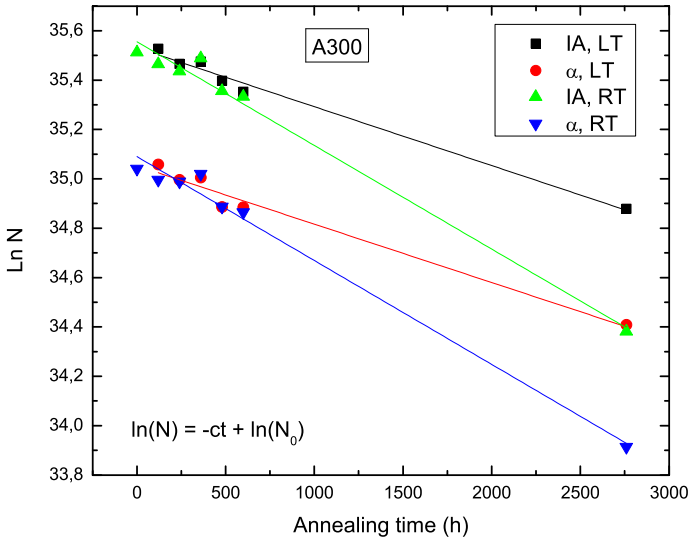

Figure 5.32: Dimer concentration versus annealing time for sample A300.

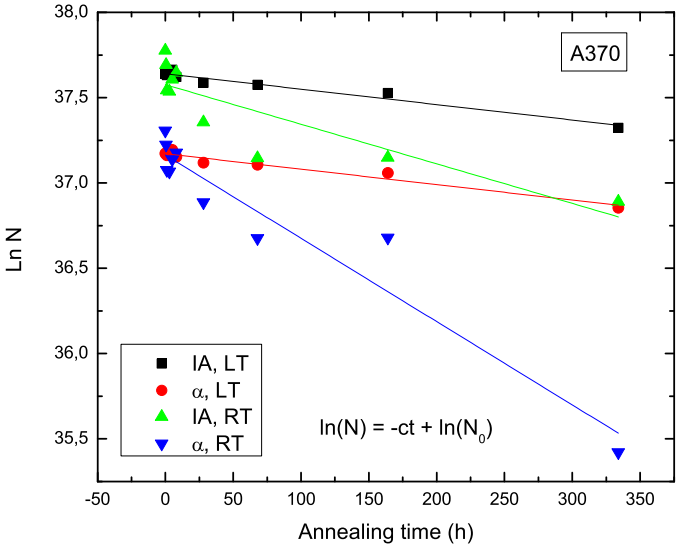

Figure 5.33: Dimer concentration versus annealing time for sample A370.

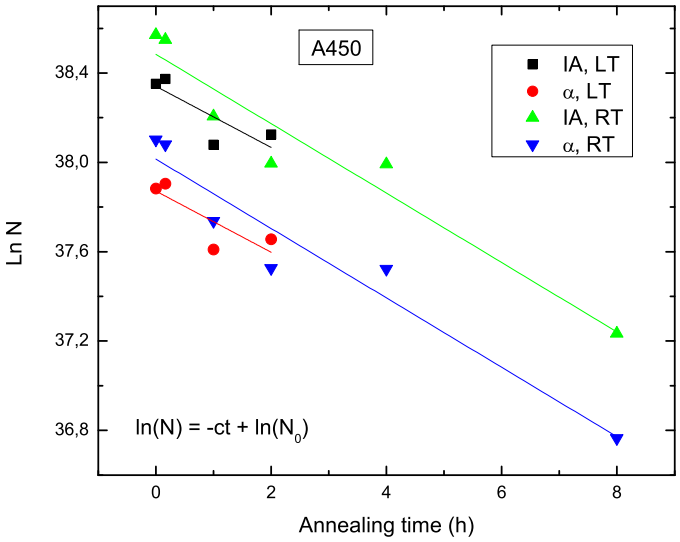

Figure 5.34: Dimer concentration versus annealing time for sample A450.

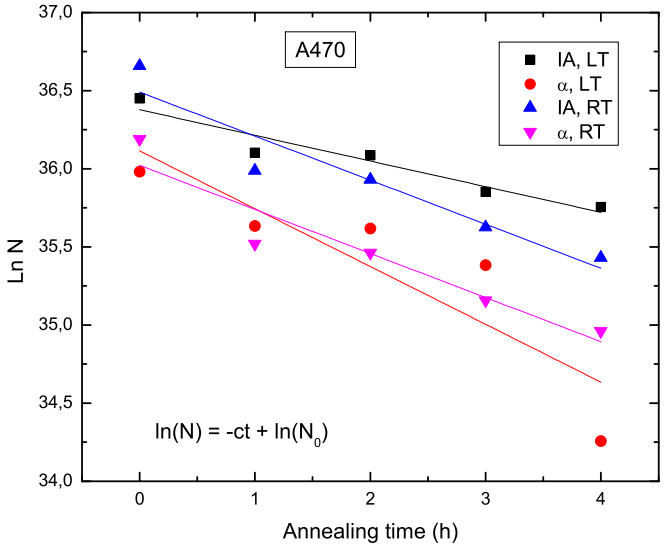

Figure 5.35: Dimer concentration versus annealing time for sample A470.

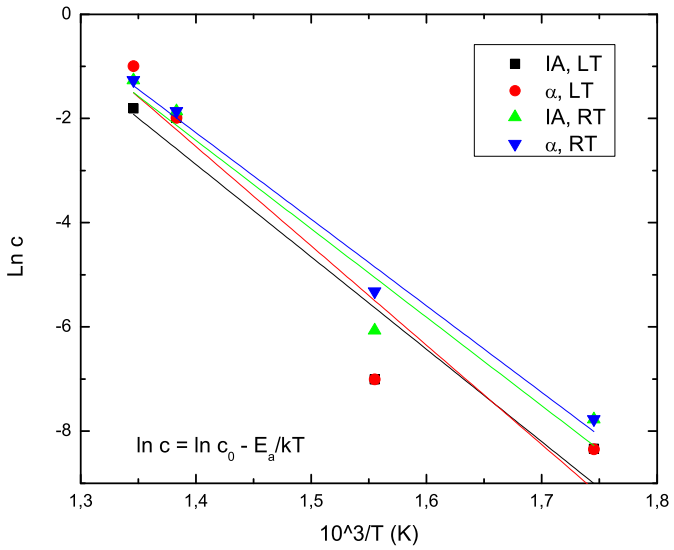

Figure 5.36: E_a was found from the slope of the Arrhenius plot and were 1.4-1.6 eV.

c_0 for a reaction, where dimers dissociation dominates, should be between 10^{12}-10^{13} s^{-1}, which is lower than what extracted. Thus, dissociation is excluded as a potential reaction. An other possible reaction can therefore be dimer diffusion to be captured by a O_i to form a complex.

E_a was found to be about 1.4-1.6 eV. Adey et al. [39] proposed that the dimer diffusion activation energy should be 0.3 eV, but since the Bourgoin-Corbett diffusion mechanism that they based their investigation on is recently questioned [27], this energy could be incorrect. Previously, Aaberg el al. [23], reported a dimer diffusion activation energy of 1.3 eV, but their samples contained high concentrations of hydrogen, which have affected their results. Senkader et al. [55] investigated dislocation locking by oxygen atoms in the temperature range 350-700°C, and did a theoretical study of oxygen transport to dislocations, where they came to the conclusion that oxygen dimers diffuse with an activation energy of 1.7-1.9 eV.

	$\mathbf{c_0}$	$\mathbf{E_a}$
IA, LT	3.43×10^{9} s^{-1}	1.5 eV
α, LT	3.11×10^{10} s^{-1}	1.6 eV
IA, RT	1.87×10^{9} s^{-1}	1.5 eV
α, RT	1.31×10^{9} s^{-1}	1.4 eV

Table 5.2: E_a and c_0 for dimers.

A possible reaction that can occur is

$$O_{2i} + O_i \rightarrow O_{3i} \tag{5.5}$$

where the dimer atom diffuses and gets trapped by an O_i atom to form a complex. Since $[O_i] >> [O_{2i}]$ the reaction rate becomes [28]

$$-\frac{d[O_{2i}]}{dt} = 4\pi RD[O_i][O_{2i}], \tag{5.6}$$

where R is the capture radius of dimers of about 5 Å and D is the diffusion coefficient. c_0 is then:

$$c_0 = 4\pi RD_0[O_i], \tag{5.7}$$

where D_0 is the pre-factor of D and was estimated to about 5.5×10^{-3}-5.0×10^{-2} cm^2/s.

The reaction rate constant tells something about how likely a reaction is going to happen. A comparison of rate constants of the O_i and O_{2i} contributions in equation 5.5 is therefore made. The diffusion for interstitial oxygen is given by [56]:

$$D(O_i) = 0.13e^{-2.53eV/k_Bt}cm^2s^{-1} \tag{5.8}$$

where $D(O_i)$ is the diffusion constant for interstitial oxygen. At 300°C, $D(O_i) = 7.26\times10^{-24}$ cm^2/s. The reaction rate constant, c(573K), can then be extracted from

$$c(573K) = 4\pi RD(O_i)[O_i] \tag{5.9}$$

and is about 4.56×10^{-12} s^{-1} . The diffusion constant for dimers is

$$D(O_{2i}) = 5.5 \times 10^{-3} e^{-1.5eV/k_B t} cm^2 s^{-1} = 3.5 \times 10^{-16} cm^2/s, \qquad (5.10)$$

which gives a reaction rate constant of c(573K)(O_{2i}) = 2.2×10^{-4} s^{-1}. The reaction rate for dimer diffusion is much higher than that of oxygen, which means that that the reaction that occur can come from dimers diffusion for then being captured by an oxygen atom to form a complex, and not the opposite, at 300°C. At 400°C the rate constant increases and the reaction goes faster.

5.8 Four point probe measurements

To see how the resistivity changes in the samples with annealing time, FPP measurements were done and the results are presented in table 5.3. The probe spacing was 0.1 cm and sample A350 and A400 were measured after annealing for 128 h and 64 h, respectively. The samples had a resistivity of about 50 Ωcm before the annealing had started.

From previous investigations it has been shown that when donor doping in a n-type semiconductor material is enhanced, the material will experience a decrease in resistivity [57]. For a p-type materal, the resistivity will initially increase and then decrease when the concentration of TDDs starts to exceed that of the p-type dopants. The resistivities measured by FPP are given in table 5.3 and show a reduction, as expected. The reason for this comes most likely from TDDs appearing in the sample, making it more n-type. This is in consistency with the results from Claybourn and Newman [58], who investigated the resistivity of Cz-Si and observed that the resistivity decreased with increasing TDD concentration.

Sample	**Current, mA**	**Voltage, mV**	**Resistivity, Ωcm**
A350(128h)	0,900	1,435	1,002
	0,800	1,276	1,002
A400(64h)	0,900	1,383	0,966
	0,800	1,229	0,965
	1,000	1,539	0,967

Table 5.3: Table over the FPP measurement results

Chapter 6

Summary

6.1 Conclusion

Irradiated n-doped Cz-Si samples, with oxygen concentration of about 10^{18} cm^{-3}, were investigated with FTIR. They were annealed at temperatures from 300-470°C and several vibrational and electronic transition bands were seen.

VO_2 (889 cm^{-1}) and VO_3 (905, 969 and 1001 cm^{-1}) bands were seen at RT measurements. It was shown that the VO_2 center decreased as the VO_3 increased in amplitude with increasing annealing time, and the two centers show a linear relation.

The 1107 cm^{-1} interstitial oxygen band were seen in RT measurements, and the concentration was monitored and calculated with annealing time. Spectra before and after irradiation were compared and showed a decrease in O_i and an increase in dimer concentration, due to dimer formation. After annealing, the 1107 cm^{-1} band decreased with increasing annealing time, where O_i atoms most likely form complexes like TDDs and VO_3 centers.

TDD bands were seen after annealing and arise from electron transition bands when measured at LT. Dimers are believed to be the precursors of these complexes, their vibrational bands decrease with annealing time and

are found at 556, 1012 and 1060 cm^{-1}. The 556 cm^{-1} band was monitored and the amplitude showed an exponential dependency with increasing annealing time. Dimer concentrations were extracted from the 1012 cm^{-1} band and it also showed an exponential dependency with annealing time.

E_a was extracted and estimated to be 1.4-1.6 eV, with a pre-factor of around 3.1×10^{10}-3.43×10^{9} s^{-1}, which gave a D_0 of 5.5×10^{-3}-5.0×10^{-2} cm^2/s. From this it is suggested that dissociation can be excluded and diffusion can be considered as the most likely reaction that occurs when the dimer concentration decreases.

FPP measurements were done on two of the samples after annealing for 64 h and 128 h and showed a decrease in resistivity, which means that the donor concentration had increased and the samples had become more n-type. This comes from the TDD complexes generated in the sample after annealing.

6.2 Suggestions for further work

Samples must be mounted carefully on the sample holder at each measurement, to avoid changes in the amplitude of the peaks due to a not homogeneous distribution of oxygen in the sample.

Dimer concentration calculations can be done with more accuracy if the baseline and the modeling function could be done in the same software at the same time, which will give less uncertainty in the values.

When E_a was extracted, only four of the six samples could be used, due to measurement issues with two of the samples. Annealing additional samples with different temperatures could give a more accurate value and a more conclusive determination of the reaction kinetics. More investigations should be done on the dimer E_a and diffusion, to unveil what happens to dimers when annealed and how TDDs are formed. Also, it could be interesting to monitor the hydrogen and carbon concentrations in the samples, to exclude

this as an influencing factor on E_a.

Appendix A

Additional spectra

A.1 1012 cm^{-1} dimer bands

The evolution of the 1012 cm^{-1} dimer band with annealing time is given in figure A.1, A.2, A.3 and A.4 for samples A300, A370, A450 and A470.

A.2 556 cm^{-1} dimer bands

Change in amplitude of the 556 cm^{-1} band for A450, A470 and A370 were found at LT and RT. The 556 cm^{-1} band is hard to study, because of the small and decreasing amplitude (around 0.05-0.2 cm^{-1}). This can be seen in figure A.5, A.6 and A.7. As the annealing time increase the peak decrease and is finally swallowed by the noise.

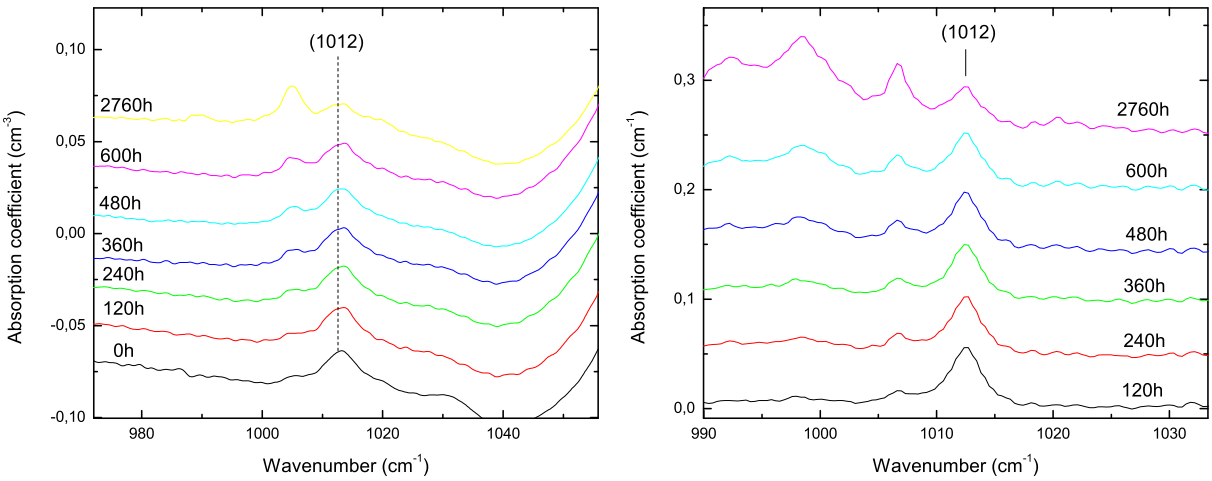

(a) 1012 cm^{-1}, RT (b) 1012 cm^{-1}, LT

Figure A.1: Change in amplitude of the 1012 cm^{-1} band for A300 annealed at 300°C.

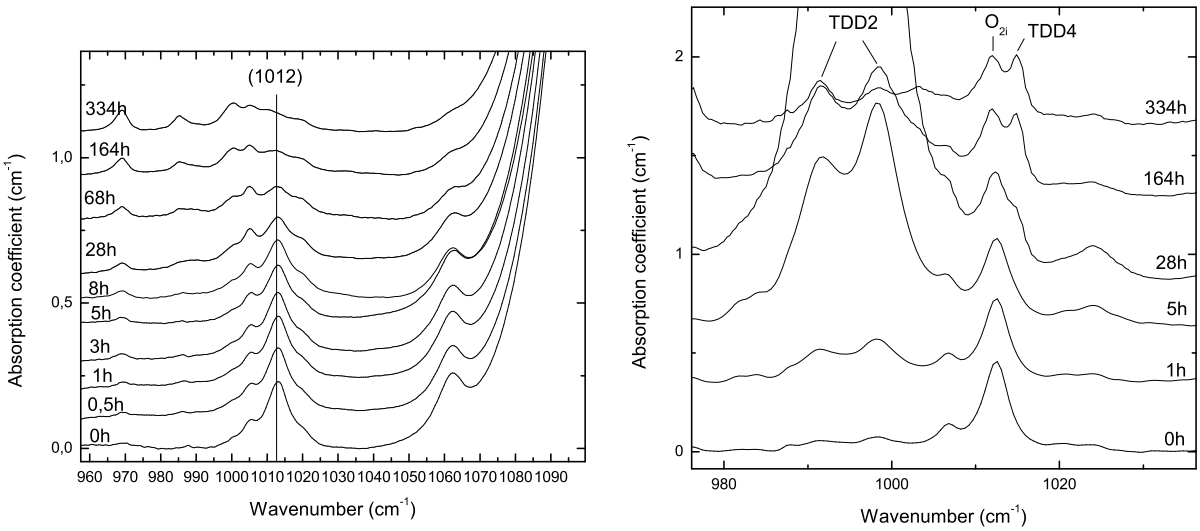

(a) 1012 cm^{-1}, RT (b) 1012 cm^{-1}, LT

Figure A.2: Change in amplitude of the 1012 cm^{-1} band for A370 annealed at 370°C.

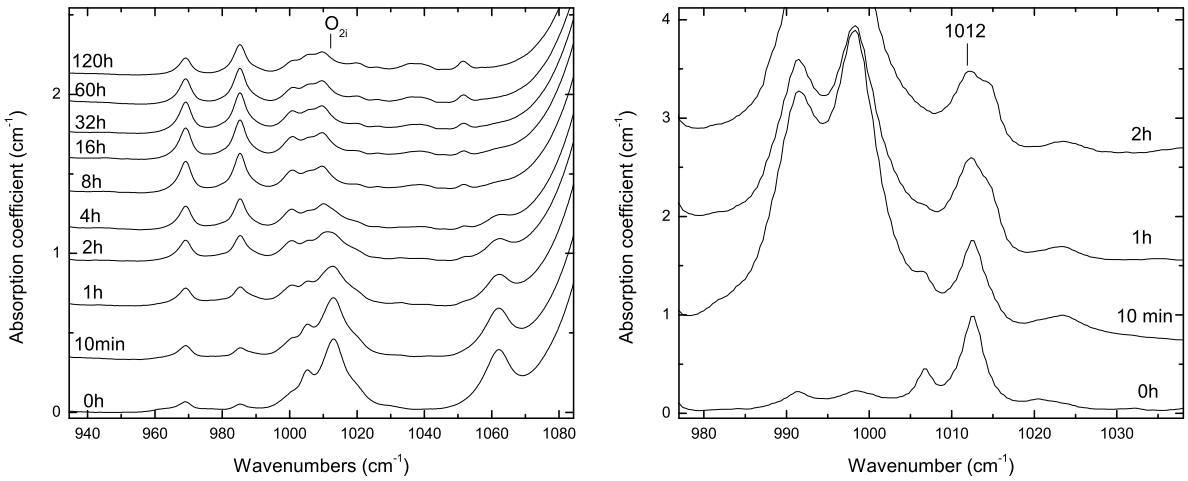

(a) 1012 cm^{-1}, RT (b) 1012 cm^{-1}, LT

Figure A.3: Change in amplitude of the 1012 cm^{-1} band for A450 annealed at 450°C.

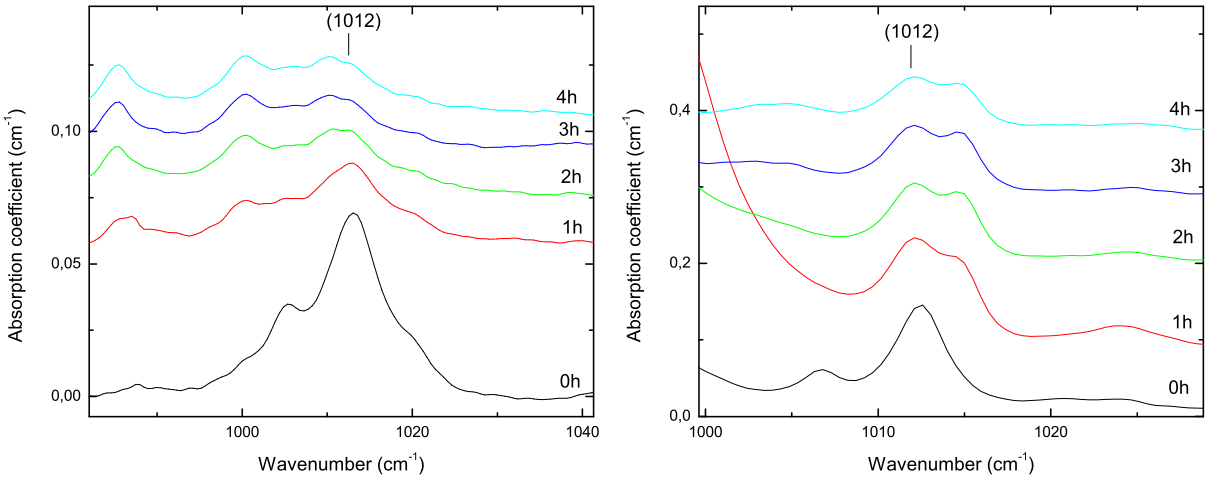

(a) 1012 cm^{-1}, RT (b) 1012 cm^{-1}, LT

Figure A.4: Change in amplitude of the 1012 cm^{-1} band for A470 annealed at 470°C.

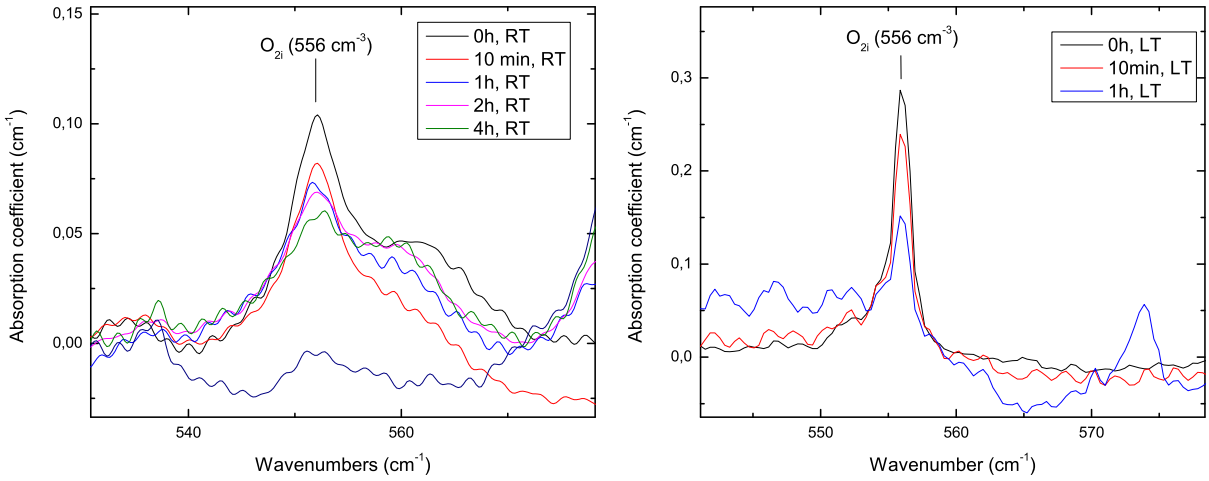

(a) 556 cm^{-1}, RT (b) 556 cm^{-1}, LT

Figure A.5: Change in amplitude of the 556 cm^{-1} band for A450.

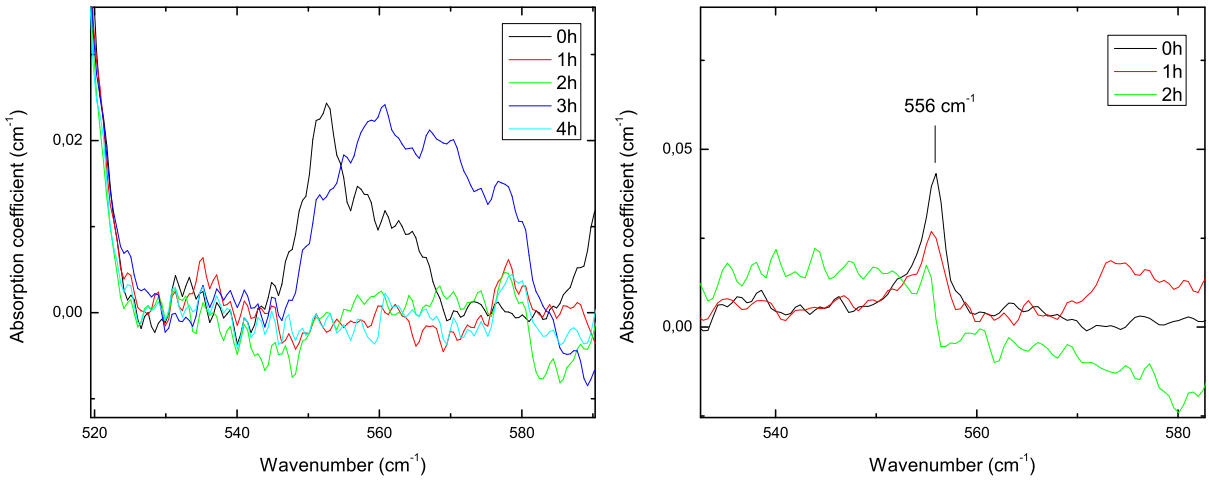

(a) 556 cm^{-1}, RT (b) 556 cm^{-1}, LT

Figure A.6: Change in amplitude of the 556 cm^{-1} band for A470.

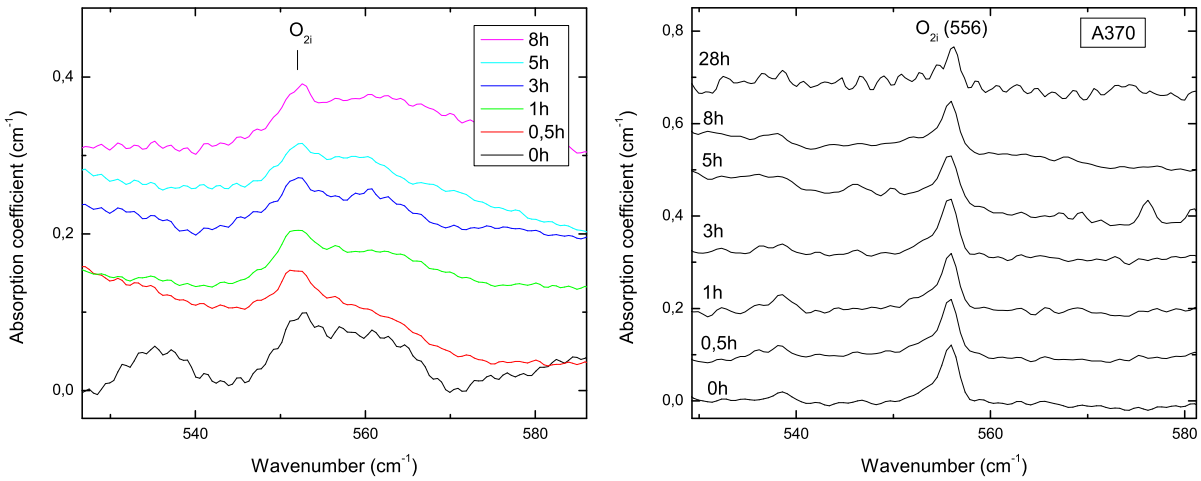

(a) 556 cm^{-1}, RT (b) 556 cm^{-1}, LT

Figure A.7: Change in amplitude of the 556 cm^{-1} band for A370.

Bibliography

[1] B. G. Streetman and S. K. Banerjee. *Solid State Electronic Devices.* Pearson Prentic Hall, 2009.

[2] Fumio Shimura, editor. *Oxygen in Silicon.* Academic Press, Inc, 1994.

[3] W. Kaiser. Electrical and Optical Properties of Heat-Treated Silicon. *Phys. Rev.*, 105(6):1751–1756, Mar 1957.

[4] W. Kaiser, H. L. Frisch, and H. Reiss. Mechanism of the Formation of Donor States in Heat-Treated Silicon. *Phys. Rev.*, 112(5):1546–1554, Dec 1958.

[5] C. Kittel. *Introduction to Solid State Physics.* John Wiley & Sons, Inc, 2005.

[6] R. J. D. Tilley. *Understanding solids: the science of materials.* Wiley, 2004.

[7] P.R. Griffiths and J.A. De Haseth. *Fourier transform infrared spectrometry.* Wiley-Interscience, 2007.

[8] A. R. Bean and R. C. Newman. The effect of carbon on thermal donor formation in heat treated pulled silicon crystals. *Journal of Physics and Chemistry of Solids*, 33(2):255–268, 1972.

[9] W. Götz, G. Pensl, and W. Zulehner. Observation of five additional thermal donor species TD12 to TD16 and of regrowth of thermal donors

at initial stages of the new oxygen donor formation in Czochralski-grown silicon. *Physical Review B*, 46(7):4312–4315, 1992.

[10] L. I. Murin, V. P. Markevich, J. L. Lindström, and M. Kleverman. Spectroscopic observation of the TDD0 in silicon. *Physica B: Condensed Matter*, 340:1046–1050, 2003.

[11] P. Wagner and J. Hage. Thermal double donors in silicon. *Applied Physics A: Materials Science & Processing*, 49(2):123–138, 1989.

[12] B. Pajot. *Optical Absorption of Impurities and Defects in Semicondicting Crystals*. Springer, 2010.

[13] W. Götz, G. Pensl, W. Zulehner, R. C. Newman, and S. A. McQuaid. Thermal donor formation and annihilation at temperatures above 500°C in Czochralski-grown Si. *Journal of Applied Physics*, 84:3561, 1998.

[14] O. Prakash, N. K. Upreti, and S. Singh. Behaviour of oxygen in CZ-silicon during 430-630°C heat treatment. *Materials Science and Engineering B*, 52(2-3):180–184, 1998.

[15] A. Kanamori and M. Kanamori. Comparison of two kinds of oxygen donors in silicon by resistivity measurements. *Journal of Applied Physics*, 50:8095, 1979.

[16] S. Singh, R. Singh, and B. C. Yadav. Thermal donor formation in CZ-silicon with reference to dimers, trimers and VO interaction. *Physica B: Condensed Matter*, 404(8-11):1070–1073, 2009.

[17] H. Navarro, J. Griffin, J. Weber, and L. Genzel. New oxygen related shallow thermal donor centres in Czochralski-grown silicon. *Solid State Communications*, 58(3):151–155, 1986.

[18] U. Gösele and T. Y. Tan. Oxygen diffusion and thermal donor formation in silicon. *Applied Physics A: Materials Science & Processing*, 28(2):79–92, 1982.

[19] L. I. Murin, T. Hallberg, V. P. Markevich, and J. L. Lindström. Experimental Evidence of the Oxygen Dimer in Silicon. *Physical review letters*, 8, 1998.

[20] T. Hallberg, J. L. Lindströem, L. I. Murin, and V. P. Markevich. The oxygen dimer in silicon: some experimental observations. In *Materials Science Forum*, volume 258, pages 361–366. Trans Tech Publ, 1997.

[21] S. Öberg, C. P. Ewels, R. Jones, T. Hallberg, J. L. Lindström, L. I. Murin, and P. R. Briddon. First Stage of Oxygen Aggregation in Silicon: The Oxygen Dimer. *Physical Review Letters*, 81(14):2930–2933, 1998.

[22] J. L. Lindström, T. Hallberg, D. Aaberg, B. G. Svensson, L. I. Murin, and V. P. Markevich. Formation of oxygen dimers in silicon during electron-irradiation above 250°C. In *Materials Science Forum*, volume 258, pages 367–372. Trans Tech Publ, 1997.

[23] D. Aaberg, B. G. Svensson, T. Hallberg, and J. L. Lindström. Kinetic study of oxygen dimer and thermal donor formation in silicon. *Physical Review B*, 58(19):12944–12951, 1998.

[24] M. Needels, J. D. Joannopoulos, Y. Bar-Yam, and S. T. Pantelides. Oxygen complexes in silicon. *Phys. Rev. B*, 43(5):4208–4215, Feb 1991.

[25] M. H. Du, H. M. Branz, R. S. Crandall, and S. B. Zhang. Bistability-Mediated Carrier Recombination at Light-Induced Boron-Oxygen Complexes in Silicon. *Physical review letters*, 97(25):256602, 2006.

[26] J. Schmidt and K. Bothe. Structure and transformation of the metastable boron-and oxygen-related defect center in crystalline silicon. *Physical review B*, 69(2):24107, 2004.

[27] L. I. Murin, E. A. Tolkacheva, V. P. Markevich, A. R. Peaker, B. Hamilton, E. Monakhov, B. G. Svensson, J. L. Lindström, P. Santos, J. Coutinho, and A. Carvalho. The oxygen dimer in Si: Its relationship to the light-induced degradation of Si solar cells? *Applied Physics Letters*, 98(18):182101, 2011.

[28] BG Svensson and JL Lindström. Kinetic study of the 830 and 889 cm-1 infrared bands during annealing of irradiated silicon. *Physical Review B*, 34(12):8709, 1986.

[29] J. W. Corbett, G. D. Watkins, R. M. Chrenko, and R. S. McDonald. Defects in Irradiated Silicon. II. Infrared Absorption of the Si-*A* Center. *Phys. Rev.*, 121(4):1015–1022, Feb 1961.

[30] G. D. Watkins and J. W. Corbett. Defects in Irradiated Silicon. I. Electron Spin Resonance of the Si-*A* Center. *Phys. Rev.*, 121(4):1001–1014, Feb 1961.

[31] J. W. Corbett, G. D. Watkins, and R. S. McDonald. New Oxygen Infrared Bands in Annealed Irradiated Silicon. *Phys. Rev.*, 135(5A):A1381–A1385, Aug 1964.

[32] B. G. Svensson, J. L. Lindström, and J. W. Corbett. Growth of the 889 cm infrared band in annealed electron-irradiated silicon. *Applied Physics Letters*, 47:841, 1985.

[33] L. I. Murin and V. P. Markevich. Thermal double donors in silicon: a new insight into the problem. *Early stages of oxygen precipitation in silicon*, 17:329, 1996.

[34] L. I. Murin, E. A. Tolkacheva, V. P. Markevich, A. R. Peaker, B. G. Svensson, and J. L. Lindström. Local vibrational modes of the oxygen trimer in Si. *physica status solidi (c)*, 8:709–712, 2011.

[35] V. Dubey and S. Singh. Formation of oxygen related donors in step-annealed CZ-silicon. *Bulletin of Materials Science*, 25(7):589–592, 2002.

[36] V. Dubey and S. Singh. Role of oxygen and carbon on donor formation in step-annealed CZ-silicon. *Journal of Physics and Chemistry of Solids*, 65(7):1265–1269, 2004.

[37] H. J. Stein and S. K. Hahn. Hydrogen-accelerated thermal donor formation in Czochralski silicon. *Applied Physics Letters*, 56:63, 1990.

[38] L. I. Murin, V. P. Markevich, M. Suezawa, J. L. Lindström, M. Kleverman, and T. Hallberg. Early stages of oxygen clustering in hydrogenated Cz-Si: IR absorption studies. *Physica B: Condensed Matter*, 302:180–187, 2001.

[39] J. Adey, R. Jones, D. W. Palmer, P. R. Briddon, and S. Öberg. Degradation of Boron-Doped Czochralski-Grown Silicon Solar Cells. *Phys. Rev. Lett.*, 93(5):055504, Jul 2004.

[40] D. W. Palmer, K. Bothe, and J. Schmidt. Kinetics of the electronically stimulated formation of a boron-oxygen complex in crystalline silicon. *Physical Review B*, 76(3):35210, 2007.

[41] K. Bothe and J. Schmidt. Fast-forming boron-oxygen-related recombination center in crystalline silicon. *Applied Physics Letters*, 87:262108, 2005.

[42] D. Macdonald, F. Rougieux, A. Cuevas, B. Lim, J. Schmidt, M. Di Sabatino, and L. J. Geerligs. Light-induced boron-oxygen de-

fect generation in compensated p-type Czochralski silicon. *Journal of Applied Physics*, 105(9):093704–093704, 2009.

[43] V. V. Voronkov and R. Falster. Latent complexes of interstitial boron and oxygen dimers as a reason for degradation of silicon-based solar cells. *Journal of Applied Physics*, 107:053509, 2010.

[44] B. C. Smith. *Fourier transform infrared spectroscopy.* CRC Press, Inc., 1996.

[45] B. Pajot, E. Artacho, C. A. J. Ammerlaan, and J. Spaeth. Interstitial O isotope effects in silicon. *Journal of Physics: Condensed Matter*, 7:7077, 1995.

[46] O. De Gryse and P. Clauws. Quantification of the low temperature infrared vibrational modes from interstitial oxygen in silicon. *Journal of Applied Physics*, 87(7):3294–3300, 2000.

[47] R. C. Newman. The initial stages of oxygen aggregation in silicon: dimers, hydrogen and self-interstitials. *Early stages of oxygen precipitation in silicon*, 17:19, 1996.

[48] A. Baghdadi, W. M. Bullis, M. C. Croarkin, Y. Li, R. I. Scace, R. W. Series, P. Stallhofer, and M. Watanabe. Interlaboratory determination of the calibration factor for the measurement of the interstitial oxygen content of silicon by infrared absorption. *Journal of The Electrochemical Society*, 136:2015, 1989.

[49] Bruker Corporation. Opus 3.0.17. www.bruker.com, 1997-2000.

[50] MA OriginLab, Northampton. Origin 8.1. www.originlab.com, 1991-2009.

[51] W. Wijaranakula. Formation kinetics of oxygen thermal donors in silicon. *Applied Physics Letters*, 59(13):1608–1610, 1991.

[52] J. Svensson, B.G. Svensson, and J.L. Lindstrom. Thermal donor formation in electron-irradiated Czochralski silicon. *Applied physics letters*, 49(21):1435–1437, 1986.

[53] J. L. Lindström, L. I. Murin, B. G. Svensson, V. P. Markevich, and T. Hallberg. The VO2 defect in silicon. *Physica B: Condensed Matter*, 340:509–513, 2003.

[54] W. Kaiser and PH Keck. Oxygen content of silicon single crystals. *Journal of Applied Physics*, 28(8):882–887, 1957.

[55] S. Senkader, P. R. Wilshaw, and R. J. Falster. Oxygen-dislocation interactions in silicon at temperatures below 700°C: Dislocation locking and oxygen diffusion. *Journal of Applied Physics*, 89:4803, 2001.

[56] R. C. Newman. Oxygen diffusion and precipitation in Czochralski silicon. *Journal of Physics: Condensed Matter*, 12:R335, 2000.

[57] J.P. Colinge and C.A. Colinge. *Physics of semiconductor devices*. Springer, 2002.

[58] M. Claybourn and R. C. Newman. Thermal donor formation and the loss of oxygen from solution in silicon heated at 450°C. *Applied Physics Letters*, 52(25):2139–2141, 1988.